Global aerosol retrieval over land from Landsat imagery integrating Transformer and Google Earth Engine

Jing Wei [a,*,1], Zhihui Wang [b,1], Zhanqing Li [a,*], Zhengqiang Li [c,d], Shulin Pang [e], Xinyuan Xi [f], Maureen Cribb [a], Lin Sun [b,*]

[a] Department of Atmospheric and Oceanic Science, Earth System Science Interdisciplinary Center, University of Maryland, College Park, MD, USA
[b] College of Geodesy and Geomatics, Shandong University of Science and Technology, Qingdao, China
[c] State Environmental Protection Key Laboratory of Satellite Remote Sensing, Aerospace Information Research Institute, Chinese Academy of Sciences, Beijing, China
[d] College of Geography and Environmental Science, Henan University, Zhengzhou, China
[e] Innovation Research Center of Satellite Application, Faculty of Geographical Science, Beijing Normal University, Beijing, China
[f] College of Marine Technology, Institute for Advanced Ocean Study, Ocean University of China, Qingdao, China.

ARTICLE INFO

ABSTRACT

Landsat imagery offers remarkable potential for various applications, including land monitoring and environmental assessment, thanks to its high spatial resolution and over 50 years of data records. However, the presence of atmospheric aerosols greatly hinders the precision of land classification and the quantitative retrieval of surface parameters. There is a pressing need for reliable and accurate global aerosol optical depth (AOD) data derived from Landsat imagery, particularly for atmospheric correction purposes and various other applications. To address this issue, we introduce an innovative framework for retrieving AOD from Landsat imagery over land, which leverages the deep-learning Transformer model (named AeroTrans-Landsat) and operates on the Google Earth Engine (GEE) cloud platform. We gather Landsat 8 and 9 images starting from their launch dates (February 2013 and September 2021, respectively) until the end of 2022, which are used to construct a robust aerosol retrieval model. The global AOD retrievals are then rigorously validated across ~560 monitoring stations on land using diverse spatiotemporally independent methods. Leveraging information from multiple spectral channels, which contributes to 80 % according to the SHapley Additive exPlanation (SHAP) method, our retrieved AODs from 2013 to 2022 generally agree well with surface observations, with a sample-based cross-validation correlation coefficient of 0.905 and a root-mean-square error of 0.083. Around 86 % and 55 % of our AOD retrievals meet the criteria of Moderate Resolution Imaging Spectroradiometer (MODIS) Deep Blue expected errors $[\pm(0.05 + 20\ \%)]$ and the Global Climate Observation System $\{[max(0.03, 10\ \%)]\}$, respectively. Additionally, our model is not as sensitive to fluctuations in both surface and atmospheric conditions, enabling the generation of spatially continuous AOD distributions with exceptionally fine-scale information over dark to bright surfaces. This capability extends to areas characterized by high pollution levels originating from both anthropogenic and natural sources.

1. Introduction

Atmospheric aerosols are suspended particulate matter (PM) consisting of solid or liquid particles with diameters ranging from 10 nm to 100 μm, located chiefly in the lower atmosphere (Kaufman et al., 1997). These aerosols originate from natural processes such as volcanic eruptions, wildfires, dust storms, and anthropogenic activities, including fuel combustion, vehicular emissions, and industrial and agricultural processes. Aerosols can alter the Earth-atmosphere radiative balance by absorbing and scattering solar radiation, directly impacting ecosystems and climate (Kaufman et al., 2002; Ramanathan et al., 2001). They also indirectly influence climate change through interactions with clouds and precipitation (Li et al., 2011; Rosenfeld et al., 2014). Furthermore, in the form of fine and ultra-fine particulate matter like $PM_{2.5}$ and PM_1, aerosols significantly deteriorate air quality and pose substantial threats to public health (Fuller et al., 2022; Fuzzi et al., 2015; Kim et al., 2015;

Li et al., 2017). Therefore, accurate determination and assessment of aerosol quantity and characteristics is of utmost significance in monitoring atmospheric environmental pollution and understanding climate change dynamics.

Aerosol optical depth (AOD) is defined as the integral of a medium's extinction coefficient in the vertical direction and serves as a critical optical parameter for characterizing aerosol content and assessing atmospheric turbidity (Kaufman et al., 2002). Satellite remote sensing offers an efficient means to acquire AOD distributions across extended timeframes and broad spatial extents. At present, a multitude of mature aerosol retrieval algorithms exists, e.g., Dark Target (Levy et al., 2013), Deep Blue (Hsu et al., 2013), and Multi-Angle Implementation of Atmospheric Correction (Lyapustin et al., 2018), using atmospheric radiative transfer (ART) models. These algorithms have been successfully and operationally applied to medium- and low-spatial-resolution sun-synchronous satellite instruments, such as the Moderate Resolution Imaging Spectroradiometer (MODIS) and the Visible Infrared Imaging Radiometer Suite (VIIRS), as well as instruments on high-temporal-resolution geostationary satellites, including Himawari and the GOES-R Series (Li et al., 2019a; She et al., 2019; Wang et al., 2022), providing daily or hourly AOD products covering the entire Earth with considerable accuracy. These datasets are invaluable for real-time air quality monitoring, tracking, forecasting, and a variety of related studies, particularly in the retrieval of PM (Ma et al., 2022; Wei et al., 2021; Zhang et al., 2021).

Satellite-derived AOD serves as the primary and most crucial input for atmospheric correction, directly impacting the accuracy of quantitative remote sensing information extraction (Doxani et al., 2023; Li et al., 2019b; Vermote et al., 2016), particularly for high-spatial-resolution satellites such as the Landsat series and Sentinel-2. For instance, aerosol retrieval is present in the official Landsat product through different Atmospheric Correction Inter-comparison eXercise (ACIX-II Land) algorithms (Doxani et al., 2018, 2023), yet access to their AOD outputs are limited. In addition, physically based methods informed by an ART model have been employed to retrieve AODs at a 30-m resolution from Landsat imagery, with a particular emphasis on urban areas (Yang et al., 2022). Luo et al. (2015) developed a simple ImAero-Landsat algorithm without using look-up tables and retrieved AODs from Landsat 7 imagery, which was then applied to improve PM_{10} estimates in Beijing, China. Tian et al. (2018) retrieved AOD from Landsat 8 imagery in Beijing City by estimating surface reflectance with a bidirectional reflectance distribution function (BRDF) using the RossThick-LiSparse model. Lin et al. (2021a) improved AOD retrievals from Landsat 8 images by developing three schemes for estimating land surface reflectance and by considering four aerosol types in Beijing and Wuhan, China. They then further refined a fusion retrieval algorithm specifically designed for urban areas using Landsat 8 and Sentinel-2 imagery (Lin et al., 2021b). Kumar and Mehta (2023) introduced a simple iterative approach to enhance AOD retrievals from Landsat 8 and Sentinel-2 data by using visible and near-infrared spectral signals across diverse land surface types. Our group has also made notable contributions to facilitating AOD retrievals from Landsat 4–8 images through the construction of priori land surface reflectance databases and the determination of aerosol types using time series analyses of historical ground measurements in Beijing, China (Sun et al., 2016; Wei et al., 2017).

Conventional methods for coupled unknown variables associated with the Atmosphere-Earth system typically depend on empirical assumptions. However, the varying sensitivity of satellite signals to diverse underlying surfaces, coupled with the high spatiotemporal variability of aerosols and their compositions, could have a substantial impact on the accuracy of aerosol retrievals (Li et al., 2009; Wei et al., 2020b). The growing capacity for robust information mining and the capability to tackle intricate, nonlinear problems have led to increased applications of artificial intelligence (AI) techniques in satellite aerosol retrievals across a range of satellite platforms (Jia et al., 2022; Su et al., 2020; Tao et al., 2023; Yeom et al., 2022). However, its application to Landsat imagery is still in its early experimental stages, and only a handful of studies have been conducted thus far. For example, Liang et al. (2022) applied a range of tree-based machine-learning (ML) models to retrieve AOD from Landsat 7 and 8 scenes covering the Beijing area, utilizing prior knowledge from multiple sources as inputs. She et al. (2022) demonstrated the effectiveness of a deep neural network (DNN) model to retrieve AOD from Landsat 8 data over land, showing strong correlations with ground-based measurements. The Landsat series of satellites have been providing long-term, high-spatial-resolution, and high-quality global-scale imagery, continuously improving and updating their capabilities since the 1970s with over 50 years of continuity (Crawford et al., 2023; Wulder et al., 2022). These advantages have made Landsat an indispensable tool in a variety of applications, such as natural resources mapping, land cover change analysis, and ecological environmental monitoring (Masek et al., 2020; Wulder et al., 2019). To achieve the reliability and accuracy in these applications, high-precision AOD products are essential for effectively removing atmospheric effects through atmospheric correction.

Therefore, this study introduces a state-of-the-art powerful deep-learning (DL) model called Transformer (Vaswani et al., 2017), developed to tackle the intricate nonlinear problems associated with Atmosphere-Earth decoupling in aerosol retrievals for Landsat imagery. To enhance the model's performance, we have integrated multi-channel information, observational geometry, absorbing gases, and surface cover and elevation, resulting in innovative aerosol retrieval using the Transformer model for Landsat imagery, known as AeroTrans-Landsat. Furthermore, we utilize the eXplainable Artificial Intelligence (XAI) technique to dissect the individual contributions of various features to aerosol retrievals. Last, we automate the entire data preprocessing process on the Google Earth Engine (GEE) platform and accomplish global-scale aerosol retrievals from Landsat imagery using the Google Colaboratory (Colab) platform. We assess the model's AOD retrieval performance using a variety of independent validation methods and compare our results with those from widely used ML and DL models, and previous studies. We also verify the model's robustness by testing it in both low- and highly-polluted representative regions selected from around the world.

2. Materials and methods

2.1. Data sources

2.1.1. Landsat 8/9 imagery

The Landsat Operational Land Imager (OLI) is a multispectral instrument onboard the eighth satellite of the Landsat Data Continuity Mission, which was launched successfully on 11 February 2013. Landsat 8 (L8) OLI provides satellite data covering the spectrum from visible to shortwave infrared channels (Roy et al., 2014). L8 OLI introduces new bands for coastal aerosol (deep blue) and cirrus cloud detection bands in comparison to its predecessor, the Landsat 7 Enhanced Thematic Mapper Plus (ETM+), which ceased operations in May 2021. It also boasts improvements in imaging width (185 km × 180 km) and daily image captures (725 scenes per day), enriching the multispectral radiometric dataset and expanding the potential for capturing cloud-free scenes globally. To minimize data gaps within the Landsat record, Landsat 9 (L9) was launched on 27 September 2021, carrying the OLI-2 sensor. It closely aligns with L8 OLI in terms of spectral bands, spatiotemporal coverage, radiometry, and geometric precision, further enhancing measurement accuracy and stability while offering extended imaging capabilities (Masek et al., 2020). L9 operates in orbit alongside L8, with an 8-day orbital offset, resulting in an updated data revisit time of every 8 days and acquiring over 1400 scenes daily. To facilitate user access and utilization, the Google Earth Engine (GEE) remote sensing cloud platform provides the USGS Landsat 8/9 Collection 2 Tier 1 TOA Reflectance dataset (Crawford et al., 2023). This dataset comprises 11 discrete spectral bands, 4 observation angles, and 2 quality assessment

bands (see details in Table S1). To eliminate the influence of clouds and ensure the quality of generated training samples, we set a cloud filter value of 20 % for all images in our study. Here, we have collected all available images from L8 (~20,947 cloud-screened scenes from 2013 to 2022) and L9 (~1333 cloud-screened scenes from 2021 to 2022) worldwide since their respective launch times, matching them with ground monitoring stations on land.

2.1.2. Ground-based measurements

The AErosol RObotic NETwork (AERONET) is a global ground-based aerosol observation network capable of automated data collection (Holben et al., 1998). It has been comprised of over 1600 monitoring stations since 1992, each equipped with a CIMEL Electronique CE318 multi-band sun photometer. AERONET provides multi-channel AOD observations every 15 min, with an average uncertainty of ±2 % (Giles et al., 2019). These observations undergo different quality controls and are categorized into three quality levels: Level 1.0 (unscreened), Level 1.5 (cloud screened), and Level 2.0 (cloud screened and quality assured) (Giles et al., 2019). AERONET AOD data has been extensively employed as ground truth for the development and validation of aerosol retrieval studies (Hsu et al., 2013; Levy et al., 2013; Lyapustin et al., 2018; Wei et al., 2019a; Wei et al., 2020b).

Given the limited number of AERONET stations in China, the Sun-sky Radiometer Observation Network (SONET) has been incorporated to enrich the observation samples. SONET is closely aligned to AERONET in terms of observation instruments, spectral bands, and data quality level categorization. It provides AOD observations at 16 long-term ground stations across China, with an average uncertainty of approximately 0.25–0.5 % (Li et al., 2018). These observations have also been widely used in studies related to the development of satellite aerosol algorithms and uncertainty analysis in China (He et al., 2021; Wei et al., 2019b). In this study, we have collected AERONET (Level 2.0) and SONET (Level 1.5) AOD ground observations at a total of ~560 land sites from 2013 to 2022 (Fig. S1) for DL model training and validation.

We have also incorporated another open-access independent observation network, the Sky Scanning Monitoring Network (SKYNET), which is dedicated to research on aerosol-cloud-solar-radiation interactions (Nakajima et al., 2020). SKYNET measures both the optical and microphysical properties of aerosols across various wavelengths. SKYNET observations have undergone rigorous inter-calibration processes and have been subjected to inter-comparison with AERONET CIMEL sun-photometers and precision filter radiometers to ensure accuracy and consistency (Estellés et al., 2012). For this study, we have gathered data from a total of 31 long-term ground stations operated by SKYNET during the study period from 2013 to 2022 (Fig. S1), serving the purpose of independent validation for the DL model. Note that the three networks do not provide direct AOD observations at 550 nm. Instead, these observations are interpolated using the Ångström algorithm following our previous study (Wei et al., 2019a).

2.2. Landsat aerosol retrieval framework

In this study, we introduce a hybrid aerosol retrieval framework, which includes the development of the aerosol retrieval using Transformer for Landsat imagery (AeroTrans-Landsat) over land, along with the implementation of the automated aerosol retrieval facilitated by the Google Earth Engine (GEE) platform.

2.2.1. AeroTrans-Landsat model

Conventional physical remote sensing approaches still face challenges in aerosol retrieval (Hsu et al., 2013; Levy et al., 2013; Lyapustin et al., 2018). In contrast, AI, particularly DL, offers a promising solution to deal with these nonlinear tasks. This study introduces an advanced DL model called Transformer to minimize these effects and enhance the capability to handle nonlinear problems. Transformer, developed by Google researchers in 2017 (Vaswani et al., 2017), has been recognized

as the fourth major category of DL models, following multilayer perceptron (MLP), the convolutional neural network (CNN), and the recurrent neural network (RNN). It was originally designed for machine translation tasks and has demonstrated outstanding performance in various domains, such as image classification and text summarization (Dong et al., 2022; Liu and Lapata, 2019). However, it has seldom been applied to the field of geoscience, especially in atmospheric science. Unlike other DL models via the pixel-by-pixel approaches, Transformer utilizes sequence (time-series) processing and unique self-attention mechanisms to model long-range dependencies and global relationships within the data. Self-attention allows Transformer to weigh the importance of different parts of the input data more dynamically, which can be particularly advantageous for tasks requiring an understanding of global context. Additionally, Transformer introduces the concepts of residual connections and encoder-decoder structures, resulting in significant breakthroughs in aspects such as operational efficiency, model flexibility, and scalability (see the model structure in Fig. S2) (Vaswani et al., 2017).

Determining input variables. Aerosols exert diverse and significant influences on the top-of-the-atmosphere (TOA) reflectance across various wavelengths, with shorter wavelengths more sensitive to aerosols (Fig. S3). As a result, seven discrete spectral channels (bands 1–7) spanning from visible (deep blue) to mid-infrared wavelengths, i.e., coastal aerosol (0.443 μm), blue (0.482 μm), green (0.562 μm), red (0.655 μm), near-infrared (NIR: 0.865 μm), shortwave infrared 1 (SWIR: 1.61 μm), and mid-infrared (MIR: 2.2 μm), are selected as the primary input features for the DL model. Notably, integrating multi-band information into the DL model can also enhance its ability to differentiate between various aerosol types over land (Wei et al., 2018). Additionally, TOA reflectances observed by OLI and OLI-2 can be affected by atmospheric water vapor and ozone, with the degree of influence varying by wavelength (TOA_λ). Therefore, they are also incorporated into the model, derived from total precipitable water vapor (TH_2O) and total column ozone (TO_3) data from the Modern-Era Retrospective analysis for Research and Applications, Version 2 (MERRA-2) Single-Level Diagnostics product. Furthermore, aerosol information is also influenced by the surface bidirectional reflectance distribution function (BRDF) and observation geometry. Five angles, including solar zenith angle (SZA), solar azimuth angle (SAA), viewing zenith angle (VZA), the viewing azimuth angle (VAA), and scattering angle (Θ), are thus included. In addition, altitude (z) is a critical factor characterizing surface terrain changes, particularly rugged terrain and at high altitudes where aerosol retrievals face great challenges (Wang et al., 2019; Wei et al., 2020a) and is derived from the NASA Digital Elevation Model (DEM) 30-m product. Last, we employ the MIR vegetation index ($NDVI_{MIR}$, Eq. (1)), which is much less sensitive to aerosols (Vermote et al., 2016), to discern land-use cover and changes. In summary, 16 influencing factors related to aerosol retrieval are selected as input features in the DL model. These variables encompass information related to various aspects, including spectral reflectance (Landsat 8/9 OLI Bands 1–7 TOA reflectances), absorbing gases (water vapor and ozone), observational geometry (i.e., SAA, SZA, VAA, VZA, and Θ), and land-surface conditions (i.e., DEM and $NDVI_{MIR}$). Leveraging the strong data-mining capabilities of DL, this approach has the potential to utilize the benefits of implicit aerosol information among multiple channels and a series of auxiliary influencing factors to address the challenges of resolving complex atmospheric-surface decoupling processes, thereby enhancing the model's capability for aerosol retrieval (Li et al., 2022; Liang et al., 2022; She et al., 2022).

$$NDVI_{MIR} = \frac{NIR - MIR/2}{NIR + MIR/2} \tag{1}$$

Model construction and training. We designate ground measurements of AOD at 550 nm (AOD_m) as the ground truth (target value) and treat the abovementioned 16 continuous features as training inputs into the Transformer. The developed AeroTrans-Landsat model can be expressed as:

$$AOD_m \sim f_{Transformer}\left(TOA_{\lambda_{1-7}}, TH_2O, TO_3, SAA, SZA, VAA, VZA, \Theta, DEM, NDVI_{MIR}\right) \tag{2}$$

She et al. (2024) demonstrated the ability of the Transformer to capture the time series information utilizing 10-min observations from Himawari-8, with time-series lengths ranging from 1 to 81 and an average of 21. In contrast, our study uses Transformer to capture time series information every 16 days from Landsat over a 10-year period (2013−2022), with the frequency improved to every 8 days after the launch of Landsat 9. This approach provides more valid observations, with time-series lengths ranging from 4 to 208 and an average of 47, thereby enhancing time-series modeling. Like She et al. (2024), our model uses a 10-year time series encoded with 16 predictor variables as inputs to produce the corresponding time series AOD retrievals as outputs.

During this process, we replace the original positional encoding module, typically employed in machine translation tasks, with multi-dimensional spatiotemporal layers. These layers are represented by a 10-year time series of 16 predictor variables, encoded using three helix-shaped trigonometric month sequence vectors (Sun et al., 2022; Wei et al., 2023), accounting for the 16-day revisit period for Landsat imagery. This encoding module enhances the Transformer' ability to effectively utilize the long-term time series information recorded by Landsat. Subsequently, we stack multiple Transformer encoders and directly yield output through fully connected layers, which not only enables us to thoroughly extract hidden aerosol information from multi-dimensional features but also effectively mitigates the overfitting issue by complex models in this specific task (Vaswani et al., 2017; Dosovitskiy et al., 2021). Specifically, the final AOD (AOD_m) is obtained using a fully connected layer as the Decoder in the Transformer model, which performs linear transformations to reduce and convert the high-dimensional feature vectors from the Encoder.

During model training, we adopt the trial-and-error approach to determine the optimal hyperparameters and utilize the early stopping strategy to pinpoint the retrieval model that performs best, which can also enhance both the model's training efficiency and convergence speed (Yeom et al., 2022). In this study, we use PyTorch (Paszke et al., 2019) to build and train our DL model. The model architecture includes 2 sub-encoder layers, a hidden layer dimension of 64, and 4 heads in the multi-head attention mechanism. To further enhance learning efficiency and extract sparse features more effectively, we employ the ReLU function as the activation function between each hidden layer. Additionally, recognizing the non-uniform distribution characteristics of the AOD target reference values in the data samples, we utilize the Huber Loss function (delta = 0.2) as the loss function to measure the disparity between predicted values and target values, thereby facilitating a more reasonable adjustment of the model's training process.

2.2.2. Google Earth Engine platform

The GEE is a cloud-computing platform designed specifically to enhance the parallel processing of petabyte-scale satellite remote sensing imagery and other geographical spatial data, leveraging the powerful computational infrastructure (Gorelick et al., 2017; Tamiminia et al., 2020). Moreover, the platform offers application programming interfaces (APIs) and integrated development environments in both JavaScript and Python, empowering users to engage in customized development according to their specific needs. Users can leverage the cloud computing capabilities of GEE's backend data center to perform a variety of computations and analyses, saving a huge amount of time required for local data downloading and processing. In this study, we employ the cloud-based automated retrieval of global AOD, facilitated by the Colaboratory (Colab) platform developed by Google Research (https://colab.research.google.com/), an interactive open-source

project that provides stable GPU computing resources. By integrating with the Python API environment of GEE, the entire process of Landsat data querying, collection, processing, and retrieval is streamlined, with Google Drive serving as an intermediary.

In the online retrieval framework, initially, Landsat 8/9 Collection 2 Tier 1 TOA reflectance data on the GEE platform is filtered based on the central coordinates of AERONET and SONET sites, retaining only valid observations that coincide with the satellite overpass time within a ± 30-min window. All valid observations are averaged to establish ground-truth values for each site. Subsequently, we utilize the Landsat quality assessment (QA) band to mask out all unsuitable retrieval pixels, including those affected by clouds, cloud shadows, water, and ice/snow. We then proceed with the extraction (e.g., spectral reflectance and angle information), computation (e.g., $NDVI_{MIR}$), and pixel-to-pixel value matching of selected input features to complete the generation of training samples. To establish a robust global aerosol retrieval model, we collect all satellite images from the launches of Landsat 8 and 9 that matched ground-based monitors, encompassing a total of 22,280 cloud-screened images (Table S2). All data samples are input into the Transformer model (currently trained in Colab), which is then applied to perform the aerosol retrieval, ultimately generating the final output map. By the way, Transformer will also be integrated into the GEE platform in the near future, enabling a fully GEE-based cloud aerosol retrieval process. Last, a 5 × 5 window median filter is applied to minimize spatial noise and enhance the quality of the final retrieval (approximately 150 m in effective spatial resolution), following our previous study (Wei et al., 2017). Fig. 1 illustrates the flowchart of our proposed model for aerosol retrieval from Landsat imagery over land.

2.3. Validation method

To comprehensively assess the performance of the proposed model for global Landsat AOD retrievals, we employ two distinct categories of independent validation methods. One is the widely used ten-fold cross-validation (10-CV), a standard approach in validating AI regression tasks (Rodriguez et al., 2010). This is conducted at sample, station, and monthly levels, which involves randomly selecting 90 % of the data samples, ground monitor stations, and months of the year for training the model, while the remaining 10 % is reserved for validation (Wei et al., 2023). This process ensures that the training samples are independent of the testing samples at overall, spatial, and temporal scales. This cycle is repeated 10 times to ensure that all data samples are used as test sets in the cross-validation. These three methods collectively evaluate the overall accuracy of AOD estimates at monitoring stations and the model performance at locations and on dates where ground measurements are not available, respectively. Lastly, we have included an additional independent validation using the leave-one-station-out cross-validation (LOOCV) approach, as detailed in the study by She et al. (2024).

The other validation method is comprised of three distinct parts: First, taking into consideration the unbalanced distribution of ground monitors and the pronounced spatiotemporal clustering patterns of AOD, we evaluate the model's predictive capabilities by withholding temporal and spatial units. This entails controlling each year from 2013 to 2022 and each of the 10 geographical continents globally [defined in Fig. S1 according to Wei et al., 2019a] to conduct independent validations (withhold one year or one continent). This is accomplished by sequentially selecting all data samples from a single year or a single continent as the validation set while utilizing data samples from the remaining 9 years or 9 continents for model training. Second, we employ
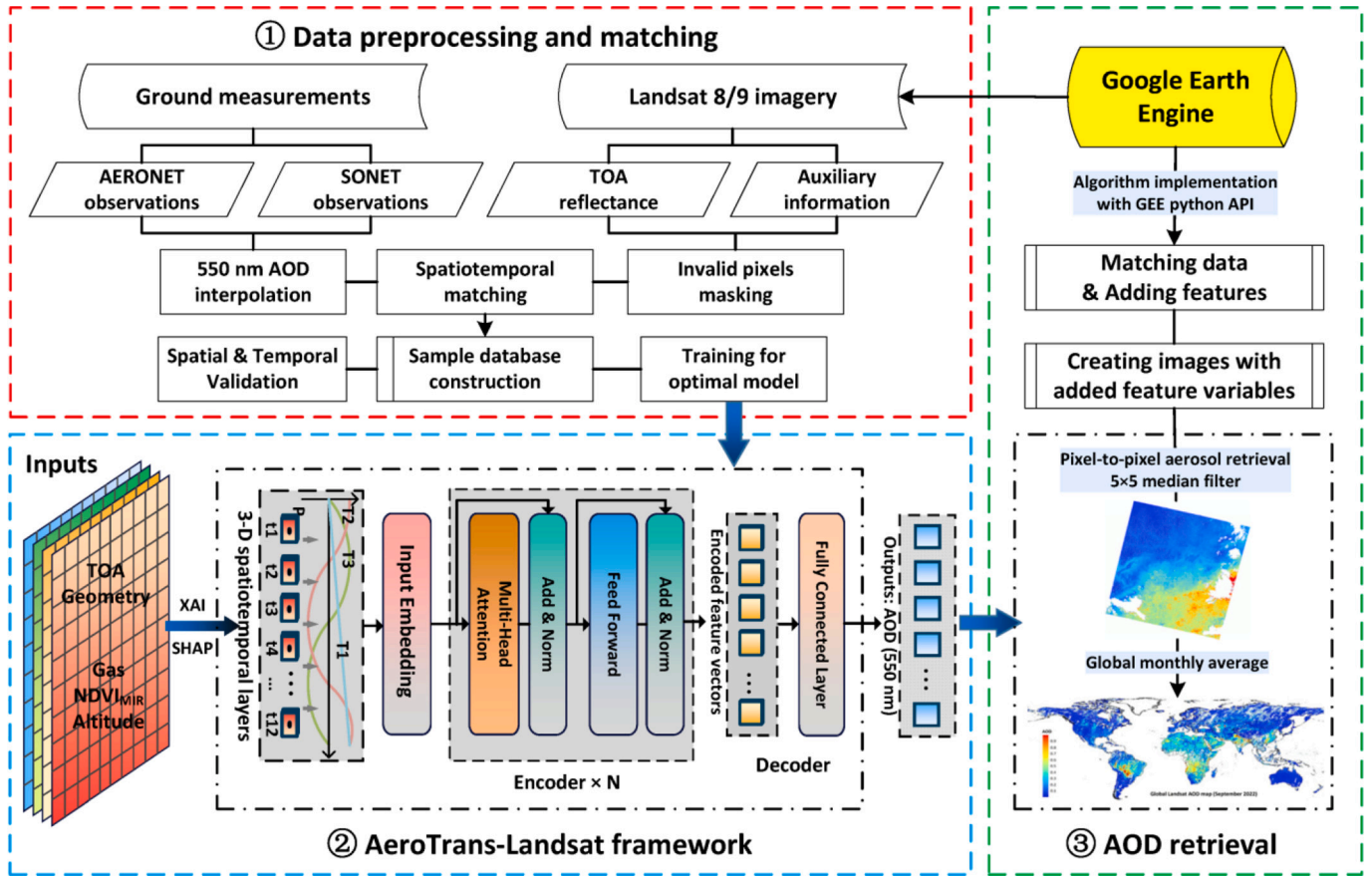
Fig. 1. Flowchart of the Transformer-informed global aerosol retrieval framework for Landsat imagery (AeroTrans-Landsat) facilitated by the Google Earth Engine (GEE) platform.

data samples from the middle 6 years (i.e., 2015–2020) for the model training and utilize the two initial years (i.e., 2013 and 2014) and the two final years (i.e., 2021 and 2022) for validation. This split results in approximately 65 % of the samples for training and 35 % for testing. This method can effectively validate the model's capacity to retrieve AOD levels in both preceding and subsequent years. Lastly, we utilize a completely independent ground-based network called SKYNET to validate the AOD retrievals for the period 2013 to 2022 produced by our developed model.

To quantitatively assess the model's accuracy and facilitate model comparison, several statistical indicators are used, namely, the Pearson correlation coefficient (*R*), median bias (MB), mean absolute error (MAE), and root-mean-square error (RMSE). Additionally, to assess the uncertainties of satellite AOD retrievals, we employ the expected errors (EE) for AOD retrievals from the MODIS Deep Blue algorithm over land (Eq. (3)) (Hsu et al., 2013) and the criteria for AOD retrievals in the Global Climate Observation System (GCOS) (Eq. (4)) (GCOS, 2010).

$$EE = \pm \left(0.05 + 20\% \times \tau_{observation}\right) \tag{3}$$

$$GCOS = \pm maximum\left(0.03, 10\% \times \tau_{observation}\right) \tag{4}$$

3. Results and discussion

3.1. Feature contribution analysis using XAI

DL models are commonly seen as black boxes, but with the emergence of XAI, their internal workings can be unveiled from a physical perspective. Here, we select the advanced SHapley Additive exPlanation (SHAP) method to calculate feature contributions for our trained model, as the Transformer itself does not have an inherent feature contribution
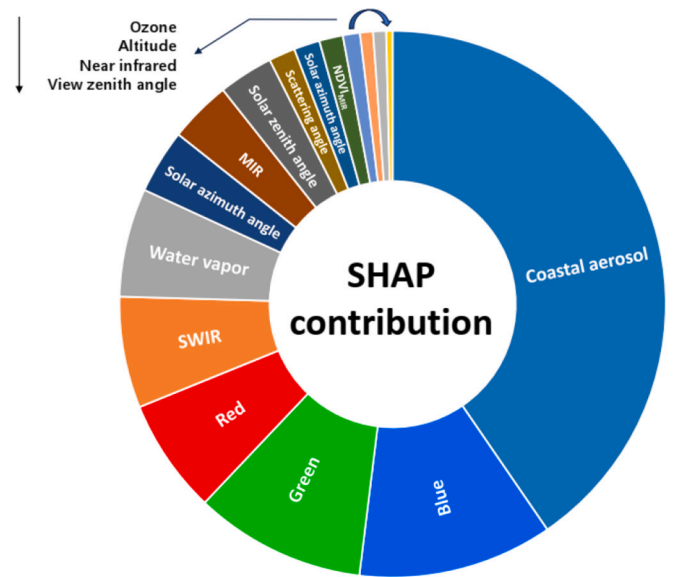

Fig. 2. Sunburst chart of feature contributions in the AOD retrieval from Landsat imagery using the SHapley Additive exPlanations (SHAP) approach of eXplainable Artificial Intelligence (XAI).

evaluation mechanism. Specifically, we utilize the Deep SHAP module, which is designed to interpret deep learning models by integrating Deep Learning Important FeaTures (DeepLIFT) and Shapley Values (Lundberg and Lee, 2017), to investigate and understand the driving factors in the

Landsat AOD retrieval (Fig. 2).

Our findings demonstrate that the coastal aerosol channel within the deep-blue wavelength exerts the most significant contribution, with the highest SHAP value of approximately 40 % among all features, followed by the blue and green channels, accounting for ~12 % and 10 %, respectively. The contributions of discrete channels to the AOD retrieval tend to gradually decrease as wavelengths increase, consistent with the decreasing sensitivity of the aerosol signal to apparent reflectance (Fig. S3). Nevertheless, these contributions remain substantial, and the total contribution of all channels, spanning from visible to shortwave infrared wavelengths, amounts to approximately 80 %, underscoring the considerable importance of multi-band information in aerosol retrievals. Observation angles, especially solar azimuth and zenith angles, also have great impacts on the AOD retrieval (total SHAP scores = 11 %). Furthermore, water vapor, NDVI$_{MIR}$, and ozone also contribute to enhancing the AOD retrieval within the Transformer model (SHAP = 1–7 %). These results illustrate the rationale behind our feature selection, contributing to a deeper understanding of the physical interpretability of DL.

3.2. Evaluation and uncertainty analysis

3.2.1. Model cross-validation

We initially employ three independent cross-validation techniques to assess the performance of the proposed model for the Landsat global aerosol retrieval. Our model demonstrates good performance in estimating AOD from Landsat images across the world, agreeing moderately well with measurements at approximately 78 % of the sites [sample-based cross-validation correlation coefficient (CV-*R*) > 0.5], with median biases within ±2 % for about 76 % of the sites (Fig. 3). Higher levels of accuracy are noted in populous areas characterized by elevated levels of air pollution, including Southern Africa, India, and East Asia

Table 1

Overall accuracy of AOD retrievals from Landsat imagery against ground-based measurements in ten continental regions of interest and on a global scale from 2013 to 2022 using the sample-based cross-validation approach.

Region	*R*	Median Bias	MAE	RMSE	= EE (%)	= GCOS (%)
EAA	0.885	0.003	0.071	0.120	78.99	40.59
SAA	0.924	0.004	0.093	0.138	80.65	41.84
SEA	0.959	0.000	0.065	0.095	84.86	44.58
EUR	0.710	0.002	0.043	0.065	85.94	51.16
ENAM	0.794	0.003	0.035	0.062	90.71	65.10
WNAM	0.871	0.001	0.037	0.071	89.27	64.63
SAM	0.906	0.003	0.035	0.054	91.00	62.25
NAME	0.823	0.001	0.080	0.129	73.31	36.13
SAF	0.932	0.004	0.042	0.059	88.24	54.45
OCE	0.666	0.002	0.027	0.043	94.80	69.90
Global	0.905	0.002	0.048	0.083	85.96	54.55

EAA: Eastern Asia; SAA: South Asia; SEA: Southeast Asia; EUR: Europe; ENAM: Eastern North America; WNAM: Western North America; SAM: South America; NAME: North Africa and the Middle East; SAF: South Africa; OCE: Oceania.

(Table 1), where correlations surpass 0.8. The retrieval uncertainties at most sites remain consistently low, with approximately 86 % and 80 % of sites having small MAE and RMSE values below 0.08 and 0.1, respectively. Exceptions are observed at a few sites in North Africa, the Middle East, and eastern China (Table 1), where larger absolute errors are primarily associated with high AOD levels resulting from heavy, frequent sand/dust emissions or anthropogenic activities. Overall, over 88 % of the sites show considerable accuracy, with more than 70 % of the retrievals falling within the EE envelope. Furthermore, 72 % of the sites have at least 40 % of retrievals meeting GCOS requirements. Similar spatial patterns are observed from spatial (temporal) CV results (Figs. S4 and S5), but the performance is generally poorer than the sample-based CV results. This is because they reflect the accuracy of the
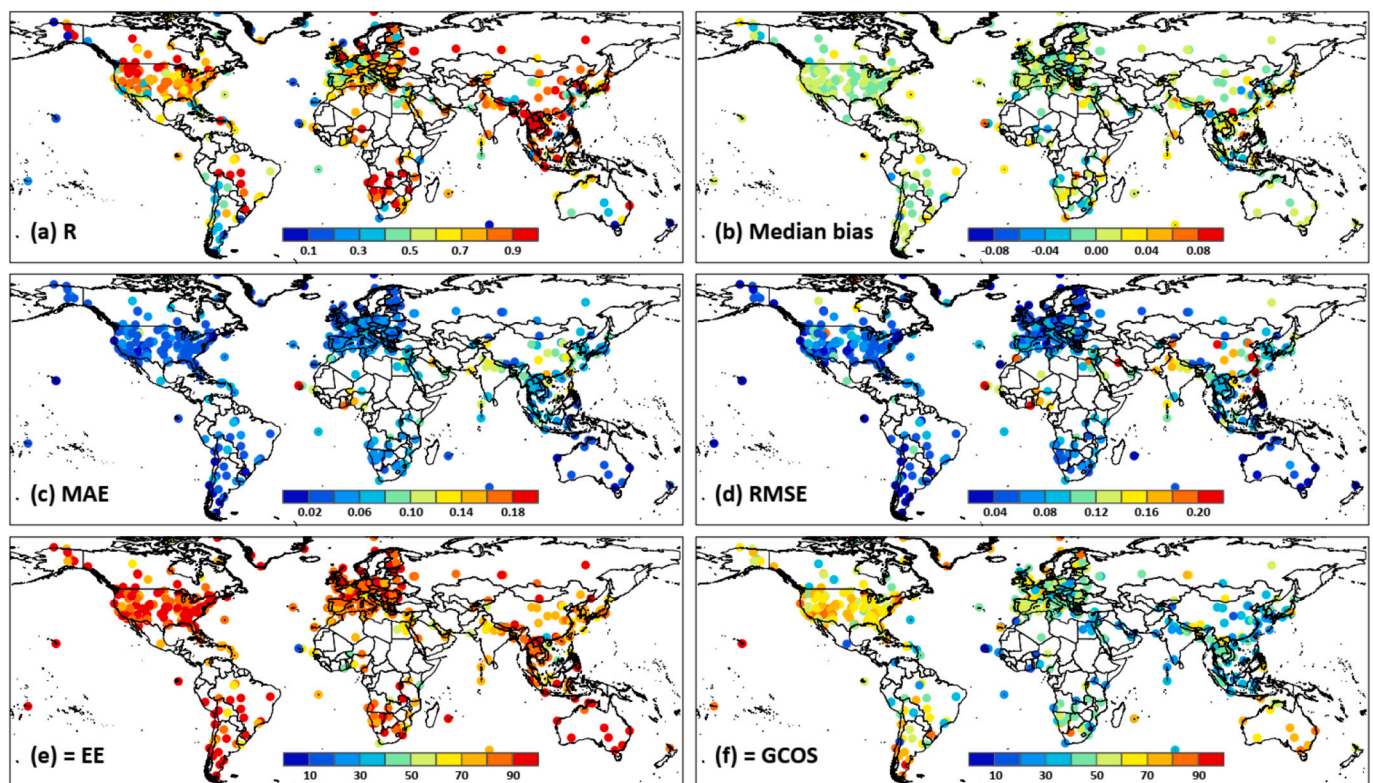

Fig. 3. Overall accuracy of AOD retrievals from Landsat imagery against ground-based measurements at the individual-site scale from 2013 to 2022 using the sample-based cross-validation approach: (a) correlation coefficient (*R*), (b) median bias, (c) mean absolute error (MAE), (d) root-mean-square error (RMSE), and the percentages of retrievals falling within the (e) expected error (EE) envelope of the MODIS Deep Blue product and (f) the uncertainty goal defined by the Global Climate Observing System (GCOS). (For interpretation of the references to color in this figure legend, the reader is referred to the web version of this article.)

model in retrieving AOD in regions or dates where observations are not available. Nevertheless, approximately 77 % (74 %), 78 % (81 %), and 72 % (74 %) of the sites continue to demonstrate station-based (month-based) moderate correlations (CV-*R* > 0.5) and low MAE (< 0.08) and RMSE (< 0.1) values between the retrievals and ground-truth values. Additionally, acceptable retrievals meeting the error criteria of the EE (> 70 %) and GCOS (> 40 %) are observed at approximately 74 % (81 %) and 52 % (65 %) of the sites on land. Despite the overall good performance at the individual-site scale, it is important to note a general trend where errors tend to increase with the decreasing density of AERONET stations, particularly in regions like Africa and the Middle East. This trend may be attributed to the limited availability of ground monitors and a smaller volume of training data acquired for the DL approach.

On a global scale, our model demonstrates exceptional overall accuracy, attaining a high CV-*R* value of 0.905. The median bias approaches zero (~0.002), and the average MAE and RMSE values remain low at 0.048 and 0.083, respectively. Approximately 86 % and 55 % of the global AOD retrievals conform to the EE and GCOS criteria (Fig. 4a). In general, our model exhibits good predictive capability on a global scale, with average station-CV (Fig. 4b) and month-CV (Fig. 4c) *R* values of 0.845 and 0.876, MAE values of 0.061 and 0.054, and RMSE values of 0.104 and 0.094, respectively. Notably, around 78 % (43 %) and 82 % (50 %) of the AOD predictions align with the EE (GCOS) anticipated deviations, respectively. Our proposed model also demonstrates exceptional performance at regional scales, especially in Southeastern, Southern, and Eastern Asia [e.g., CV-*R* = 0.83–0.96, the fraction of retrievals falling within the EE envelope (f_{EE}) = 68–85 %) (Tables 1, S3, and S4). Additionally, the leave-one-station-out cross-validation (LOOCV) results demonstrate high agreement with observations on a global scale, with indices of *R* = 0.908, RMSE = 0.082, and MAE = 0.047, respectively. These additional independent validations attest further to the robustness of our model's performance. Nevertheless, while cross-validation is a standard method for evaluating model performance, it can have limitations in regions with sparse ground measurements, such as Africa and South America. This method might not fully represent the true accuracy in these areas, as the model may exhibit limited generalizability and potential biases due to insufficient data.

3.2.2. Spatiotemporal predictability

To further assess the model's predictive ability in new spatiotemporal domains, we employ a variety of spatiotemporally independent validation methods. Initially, by isolating the spatial dependence through the independent control of each continent (withhold), our model demonstrates proficiency in predicting AOD values for various regions, where most yield moderate correlations exceeding 0.6 and maintained low median biases within ±1 % (Table S5). Furthermore, more than half to 92 % of the spatial predictions align with the EEs for each region. However, decreased performance is observed at unmonitored locations, especially in regions like North Africa, the Middle East, and Eastern Asia. This could be attributed to substantial variations in natural conditions and the influence of anthropogenic emissions (such as sand, dust, and haze) (Wei et al., 2019a; Sogacheva et al., 2020; Falah et al., 2021). Similarly, the AI method faces difficulties in accurately learning their conditions from other regions, leading to reduced performance when applying the model trained on data samples collected in other areas.

Considering the inhomogeneity of global observation sites, particularly at high latitudes above 60 degrees and local regions like Central Asia with limited sites, we conduct additional independent validations.
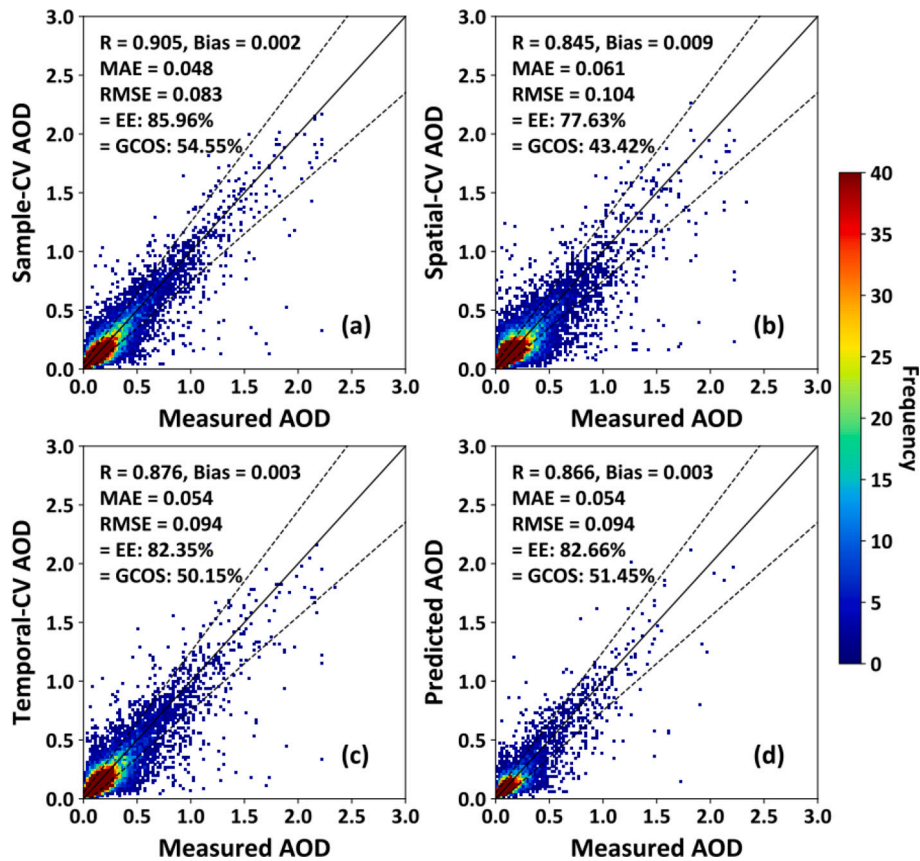

Fig. 4. Density scatter plots of global AOD retrievals derived from Landsat imagery against ground measurements over land from 2013 to 2022 using the (a) sample-based, (b) station-based, (c) month-based 10-fold cross-validation methods, and (d) the spatiotemporally independent validation method (i.e., using data samples from the years 2015 to 2020 for training and the remaining years for testing). The solid black line is the 1:1 line, and the dashed lines outline the EE envelope.

We first utilize data samples from low latitudes (within 60 degrees) for training, then employ ground measurements from 27 available AERO-NET sites at high latitudes above 60 degrees for validation. Our retrievals exhibit an average correlation of 0.811 compared to ground measurements, with average MAE and RMSE values of 0.045 and 0.096, respectively. The estimation bias is −0.003, with approximately 83 % and 57 % of retrievals meeting MODIS EE and GCOS requirements. Similar independent validation is also conducted in Central Asia, utilizing data samples from global regions excluding Central Asia for training and comparing them against available measurements at 18 sites in Central Asia. Our model performs generally well, with an average R of 0.844, MAE of 0.097, and RMSE of 0.163 between the retrievals and measurements. Additionally, approximately 70 % and 38 % of the retrievals meet EE and GCOS criteria, respectively.

By independently controlling each year (withhold) to reduce temporal correlations, our model effectively captures AOD loads for the remaining years, achieving high correlations and minimal uncertainties (e.g., R = 0.80–0.92, MAE = 0.04–0.06, and RMSE = 0.07–0.1) compared with ground measurements (Table S6). Moreover, a significant proportion of the temporal predictions, at least 82 % and 49 %, meet the EE and GCOS requirements, respectively. Furthermore, we construct the model using data samples from the years 2015 to 2020 for training, with the remaining years (2013, 2014, 2021, and 2022) utilized for testing, as illustrated in Fig. 5. Across the globe, AOD retrievals exhibit notable accuracy, with moderate correlations exceeding 0.5 at more than 78 % of the sites. Moreover, approximately 83 % and 77 % of the sites display low MAE and RMSE values of less than 0.08 and 0.1, respectively. However, in regions with elevated AOD levels, such as Africa and Eastern China, sites are more prone to underestimation, showing higher RMSE and MAE values. Nonetheless, a substantial portion (62 %) of the sites demonstrate nearly "unbiased" estimates

Table 2

Model performance in retrieving AOD from Landsat imagery in specific continental regions of interest and on a global scale using the spatiotemporally independent validation approach, i.e., data samples from the years 2015 to 2020 for training and other years for testing.

Region	R	Median Bias	MAE	RMSE	= EE (%)	= GCOS (%)
EAA	0.843	0.012	0.083	0.137	72.75	34.15
SAA	0.890	0.063	0.122	0.161	70.12	30.71
SEA	0.928	−0.004	0.077	0.110	77.86	35.71
EUR	0.610	0.001	0.047	0.075	83.96	50.30
ENAM	0.750	−0.001	0.037	0.066	89.32	64.20
WNAM	0.857	0.004	0.044	0.083	85.24	58.00
SAM	0.882	0.012	0.037	0.051	86.01	56.79
NAME	0.757	0.004	0.091	0.144	69.19	33.75
SAF	0.900	−0.001	0.049	0.068	82.95	46.51
OCE	0.549	−0.001	0.032	0.046	91.28	65.44
Global	0.866	0.003	0.054	0.094	82.66	51.45

EAA: Eastern Asia; SAA: South Asia; SEA: Southeast Asia; EUR: Europe; ENAM: Eastern North America; WNAM: Western North America; SAM: South America; NAME: North Africa and the Middle East; SAF: South Africa; OCE: Oceania.

(within ±2 %). In addition, more than 78 % and 63 % of the sites have a significant proportion of the retrievals falling within the EE (> 70 %) and GCOS (> 40 %) envelopes. Regionally, the model performance is generally acceptable, with relatively small biases (Table 2). The highest correlations are observed in Southeast Asia and Southern Africa (R = 0.928 and 0.9), while Europe and Oceania exhibit relatively lower correlations, attributable to historically clear air with low AOD loads. However, they have higher fractions of retrievals falling within the EE (~84 % and 91 %, respectively) and GCOS (~50 % and 65 %, respectively) envelopes. Our model demonstrates great predictive accuracy on a global scale, with a correlation coefficient of 0.866 between retrievals
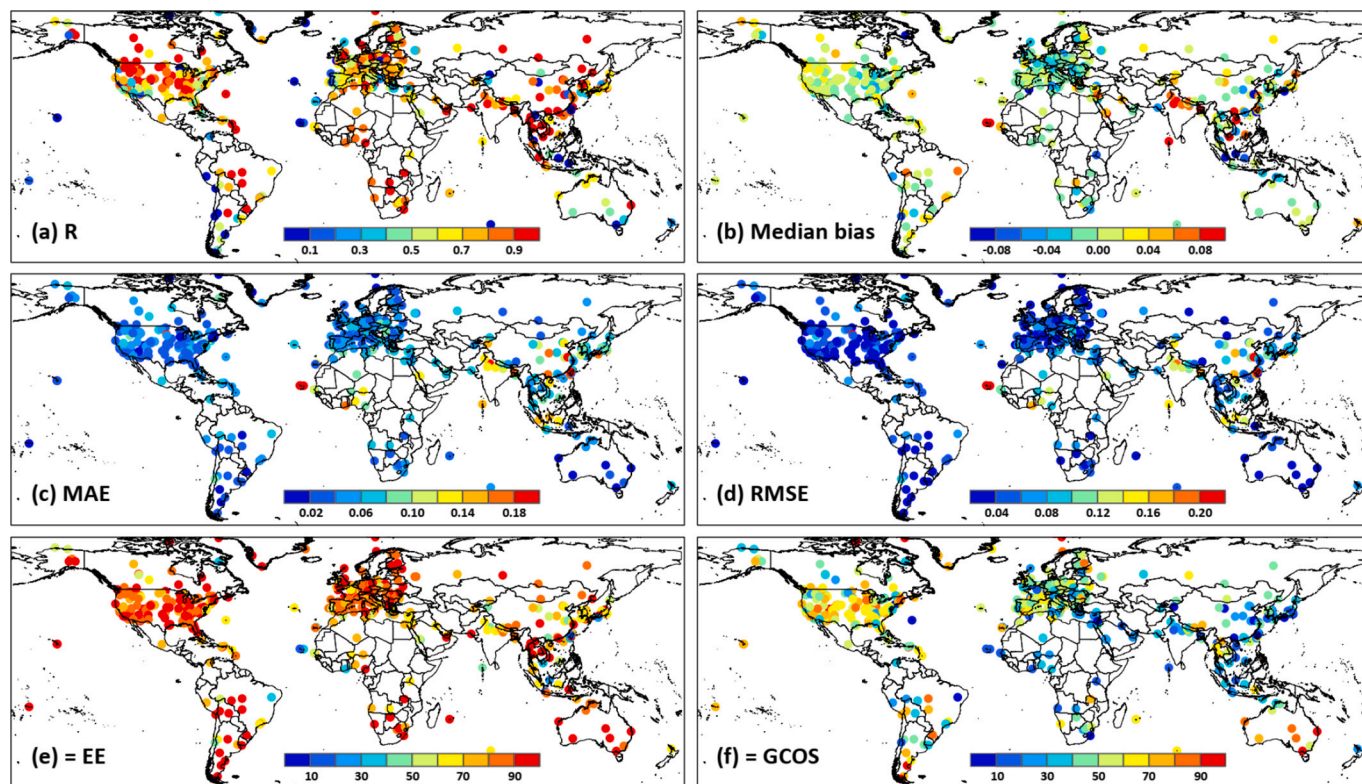

Fig. 5. Model performance in retrieving AOD from Landsat imagery against ground-based measurements at the individual-site scale from 2013 to 2022 using the spatiotemporally independent validation approach (i.e., data samples from the years 2015 to 2020 for training and other years for testing): (a) correlation coefficient (R), (b) median bias, (c) mean absolute error (MAE), (d) root-mean-square error (RMSE), and the percentages of retrievals falling within the (e) expected error envelope (= EE) of the MODIS Deep Blue product and (f) the uncertainty goal defined by the Global Climate Observing System (GCOS). (For interpretation of the references to color in this figure legend, the reader is referred to the web version of this article.)

and observations and a median bias close to zero (Fig. 4d). Average MAE and RMSE values stand at 0.054 and 0.094, respectively. Approximately 83 % of the collocated points fall within the EE envelope, and more than half (51 %) meet the GCOS requirements.

Furthermore, we employ one open-access independent global observation network, SKYNET, to validate the performance of our model in retrieving AOD from Landsat imagery for the period 2013–2022 at 31 globally distributed monitoring stations (Fig. S1). This independent validation demonstrates the reasonable ability of our proposed model to retrieve AOD in previously unobserved regions, with a median bias of −0.017. The retrievals exhibit an average R of 0.746, along with MAE and RMSE values of 0.068 and 0.105, respectively, when compared to SKYNET AOD measurements. Additionally, 74 % and 43 % of the collocated samples ($N = 1887$) satisfy the requirements of EE and GCOS, respectively.

3.2.3. Uncertainty analysis

Aerosol retrieval errors can arise from various sources. To assess the uncertainty of AOD retrievals, we examine the model's performance with respect to variations in surface and atmospheric conditions (Fig. 6). When using NDVI as an indicator of surface conditions (Fig. 6a), our model demonstrates stability in sparse and low-vegetation areas (NDVI <0.3), exhibiting median biases slightly below zero and (within) EE fractions consistently above 80 %. Moreover, as NDVI values increase, the model's overall accuracy gradually improves, with median biases approaching zero. There is also a continuous enhancement in (within) EE fractions, reaching approximately 90 % in densely vegetated areas (NDVI ≥0.6). Our model consistently delivers reliable AOD retrievals across various land-use types (Fig. 6b), particularly excelling in grassland (e.g., median bias = −0.008, and f_{EE} = 91 %) and forest (e.g., median bias = −0.007 and f_{EE} = 90 %) areas. Our model also performs effectively in retrieving AOD over bare land (e.g., median bias = −0.005, and f_{EE} = 86 %) and urban areas (e.g., median bias = −0.002, and f_{EE} = 83 %), where populations are densely concentrated amidst complex surface structures and challenging climate conditions. In low-elevation areas (< 300 m), the model exhibits stable performance with slight overall underestimations (median bias = −0.004 to −0.006) and high proportions (83–86 %) of retrievals falling within the EE envelope (Fig. 6c). Note the observed shift around the altitude range of

400 m, characterized by a narrower range of biases and a higher fraction of retrievals falling within the EE envelope, may be associated with the generally lower AOD values (average ground truth value = 0.11 ± 0.15) compared to nearby ranges of values (0.18 ± 0.22). In mid-elevation to high-elevation areas (≥ 500 m) areas, the model's performance shows gradual improvement with rising surface elevation, as indicated by the reduced variability of estimated biases and the increased fraction of retrievals falling within the EE envelope.

As surface reflectance increases, the model's performance gradually declines, with a widening range of AOD biases and a decreasing fraction of retrievals falling within the EE envelope (Fig. 6d). Nevertheless, the median bias remains relatively close to zero, and the f_{EE} consistently exceeds 80 %. The model also performs well for bright surfaces, an area where traditional physical methods have historically faced challenges due to difficulties in accurately estimating surface reflectance, leading to substantial estimation uncertainties. In regions with strongly absorbing aerosol types (single-scattering albedo, SSA < 0.9), our model maintains overall estimated median biases below 0.04, with approximately 80 % of the retrievals meeting the requirement of the EE criterion (Fig. 6e). However, as the SSA increases and aerosol absorptivity weakens, the model's estimation uncertainty gradually rises, leading to AOD retrievals tending towards underestimation, particularly for weak or non-absorbing (spheroid) aerosol types, such as dust and smoke. Nevertheless, the proportion of AOD retrievals falling within the EE envelope remains at 66 %, indicating acceptable accuracy. Furthermore, we evaluate the model's performance under varying aerosol loads (Fig. 6f). Under clean conditions (AOD < 0.1), daily AOD values are accurately retrieved, with more than 90 % of them deemed satisfactory (median bias = 0.011). However, as pollution levels increase, the model's estimation uncertainty gradually increases, and the proportion of samples meeting the EE criterion decreases, particularly under highly polluted conditions (AOD > 1), with estimation biases fluctuating over a wider range of values. Additionally, AOD values are generally underestimated, mainly due to the limited number of data samples with high values. Nonetheless, more than 72 % of retrievals still meet the MODIS EE requirements.
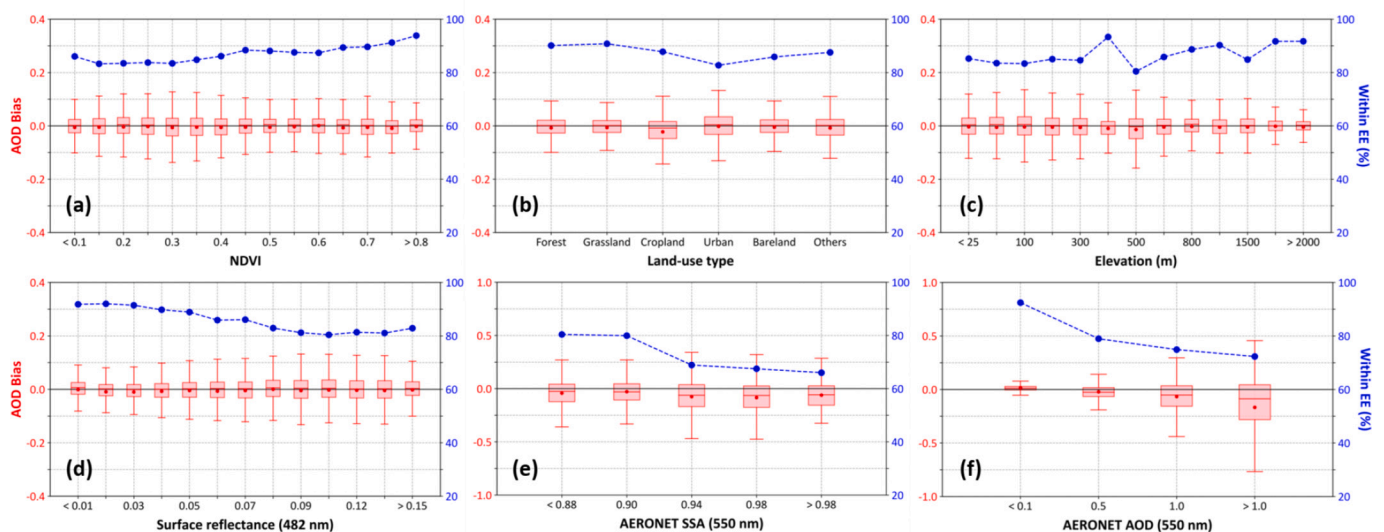

Fig. 6. Uncertainty analysis with box plots of bias and the fraction of retrievals falling within the EE envelope (curves) of global AOD from Landsat imagery retrievals against ground-based measurements for various surface conditions, including (a) NDVI, (b) land-use type, (c) elevation (m), (d) surface reflectance (482 nm), as well as atmospheric conditions, including (e) AERONET single scattering albedo (SSA, 550 nm) and (f) AOD (550 nm) measurements. Black horizontal solid lines represent zero biases. In each box, the red dot and middle, lower, and upper horizontal lines represent the AOD bias mean, the median, and the 25th and 75th percentiles, respectively. (For interpretation of the references to color in this figure legend, the reader is referred to the web version of this article.)
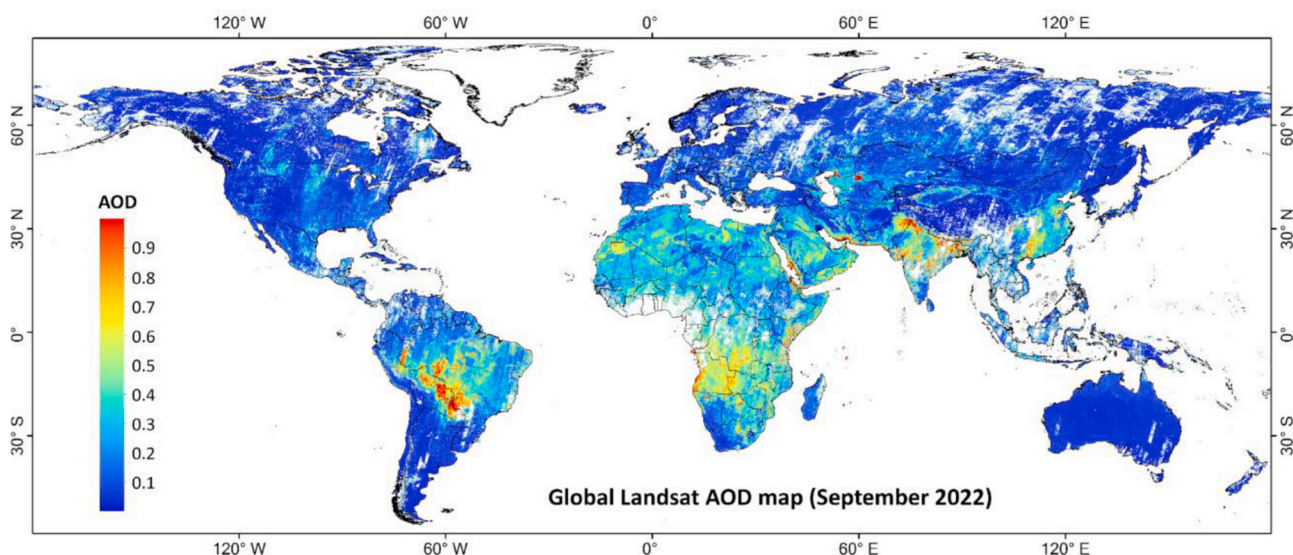
Fig. 7. Spatial distribution of high-resolution (30 m) global AOD (550 nm) over land for September 2022, derived from Landsat imagery.

3.3. Global and regional aerosol retrieval experiments

3.3.1. Mapping global AOD using Landsat imagery

Given the extensive volume of Landsat imagery available globally, this study only calculates one-month aerosol retrieval results to illustrate the global distribution and variation. Fig. 7 presents arguably the first global retrievals of monthly AOD at the highest resolution (30 m)

over all continents in September 2022 using a total of over 38,000 Landsat 8 and Landsat 9 images. Globally, AOD varies regionally, influenced by various factors. In densely populated cities and industrial areas, such as some regions in Asia like Eastern China (Beijing) and northern India (New Delhi), higher AOD values are typically observed. They are often attributed to increased pollution levels in the atmosphere due to industrial, traffic, and anthropogenic emissions (Gunthe et al.,
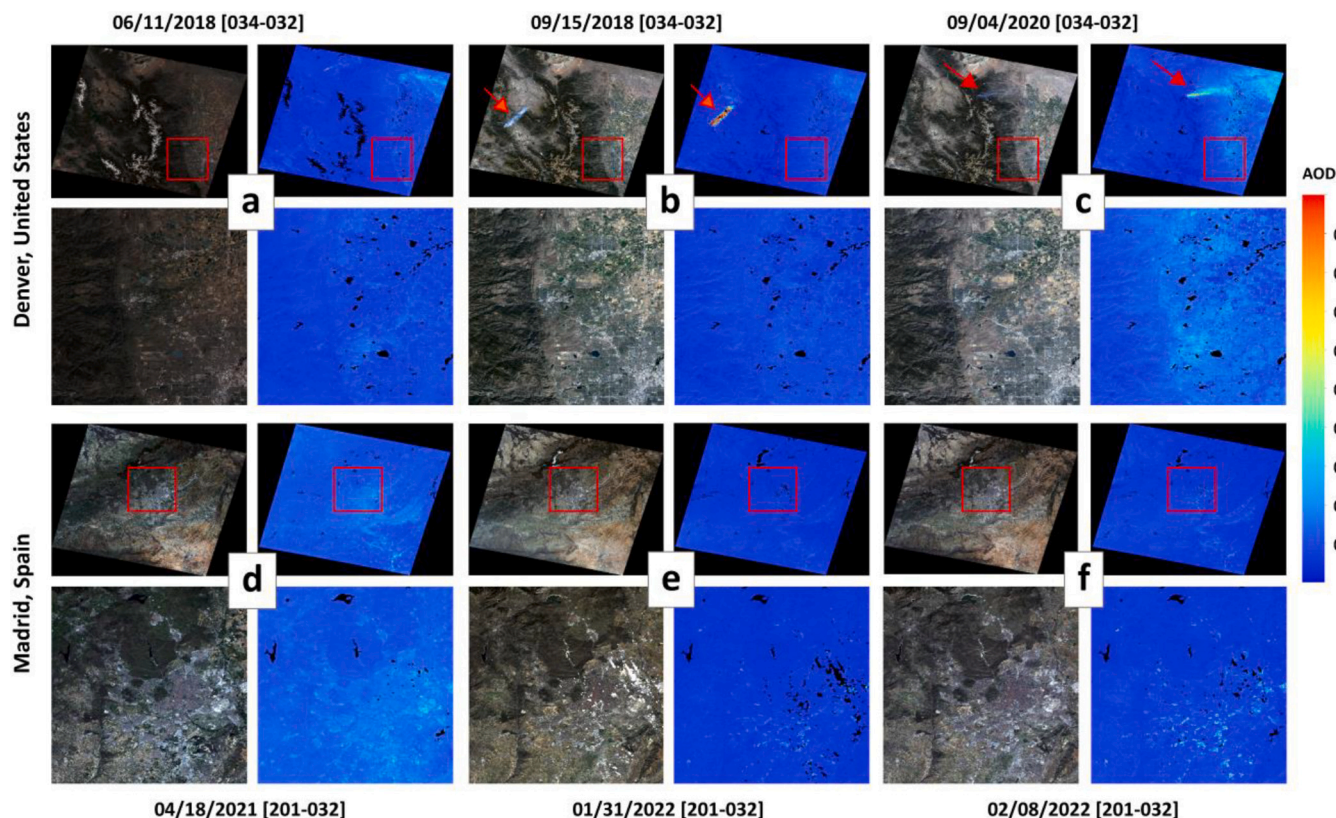

Fig. 8. Color composite (RGB: Bands 4–3–2) images and corresponding AOD retrievals (550 nm) from Landsat (AeroTrans, 30 m) and MODIS imagery (MAIAC, 1 km) for full-scene and zoomed-in core-region views (areas outlined in red) under clear conditions: (a-c) Denver, US and (d-f) Madrid, Spain. Identified unsuitable pixels for aerosol retrievals (e.g., clouds and snow/ice) are in black in the two rightmost images, and the top and bottom annotations indicate acquisition times (mm/dd/yyyy, where yyyy = year, mm = month, and dd = day) and orbital records (path-row) of the Landsat images. (For interpretation of the references to color in this figure legend, the reader is referred to the web version of this article.)

2021; Wei et al., 2023; Chen et al., 2024). Additionally, seasonal meteorological conditions also affect the spatial distribution of AOD. In September, some regions like central South America and central Southern Africa typically experience large-scale wildfires and biomass burning, releasing smoke and PM into the atmosphere, thereby increasing AOD values. Furthermore, tropical cyclones and storms may trigger widespread dust storms in some areas, further elevating AOD values, especially in desert regions like the Sahara Desert in North Africa. By contrast, in a variety of remote or cleaner areas, such as the United States (US), Canada, Europe, and Australia, AOD values are much lower. These regions are typically distant from industrial pollution sources and are influenced by clean oceanic air currents. Our retrievals also exhibit a high consistency in spatial patterns with the MODIS 1-km Multi-Angle implementation of Atmospheric Correction (MAIAC) AOD product (Fig. S6), particularly in regions with high AOD loadings. However, differences may arise due to variations in sampling accuracy stemming from the significant difference in revisit cycles (half a month versus once or twice a day).

3.3.2. Landsat AOD retrieval over typical regions

Here, two clear regions and four polluted regions are selected for further examination. These regions encompass diverse land-use types and serve as representatives of varying surface conditions, climates, and levels of human activity. All available Landsat 8/9 OLI images from

these regions from 2013 to 2022 are collected to conduct aerosol retrievals using our developed model. Fig. 8 presents true-color images and corresponding AOD retrievals (550 nm) from Landsat imagery for Denver, US, and Madrid, Spain, on different dates, both illustrative examples of clean conditions. These regions share similar land surface characteristics, primarily comprising plains and mountains, dense vegetation (forests, grasslands, croplands), low population densities, and consistently low aerosol levels throughout the year. Our model exhibits high spatial continuity and provides detailed pollution information at a high spatial resolution (30 m), capturing subtle spatial variations within the overall low aerosol background throughout the months. Importantly, the model is capable of capturing high smoke AOD values generated by sudden small wildfires on specific days (e.g., 15 September 2018 and 4 September 2020) during the fire season in Denver, US, even across the entire image at relatively low pollution levels (red arrows in Fig. 8b-c). We also validate the aerosol retrievals using data from 12 available AERONET stations within the two study areas. A high level of agreement between observations and retrievals is revealed, with estimated median biases less than ±1 % and close RMSEs equal to 0.05–0.06. Approximately 90 % and 88 % of the retrievals meet the EE criterion, with proportions falling within the GCOS range of 68 % and 57 %, respectively.

Fig. 9 displays true-color images and corresponding AOD retrievals (at 550 nm) from Landsat imagery, along with a comparison to MODIS
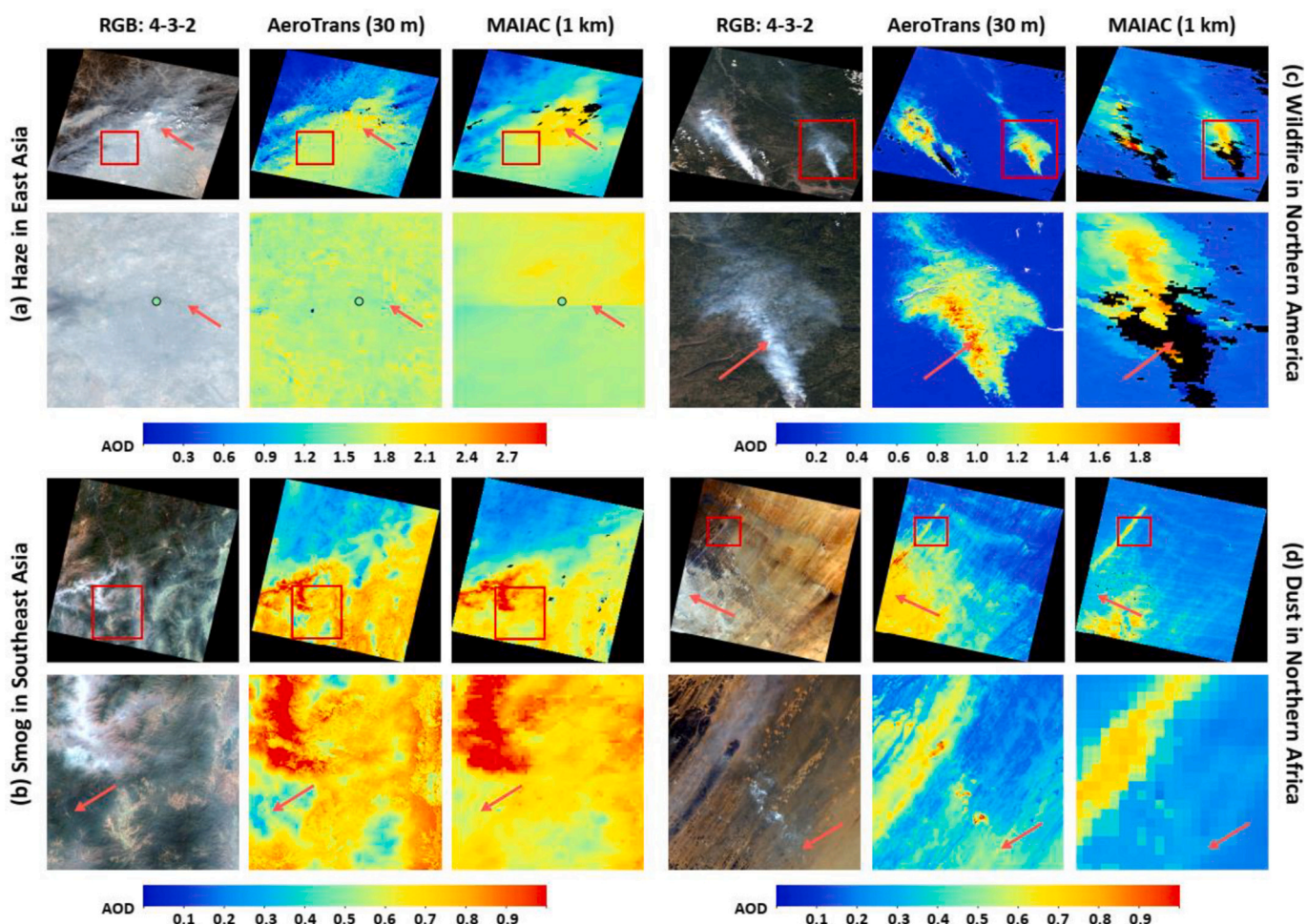

Fig. 9. Color composite (RGB: Bands 4–3–2) images and corresponding AOD retrievals (550 nm) from Landsat (AeroTrans, 30 m) and MODIS imagery (MAIAC, 1 km) for full-scene and zoomed-in core-region views (areas outlined by red boxes) under highly polluted conditions, including (a) haze in East Asia (Beijing, China), (b) smog in Southeast Asia (Chiang Mai, Thailand), (c) wildfires in North America (western US), and (d) dust in Northern Africa (the Sahara Desert). The colored dots in (a) represent ground-based measurements. (For interpretation of the references to color in this figure legend, the reader is referred to the web version of this article.)

MAIAC operational AOD products for selected regions experiencing severe pollution conditions. Beijing, China, situated in East Asia, is a densely populated city that often experiences poor air quality conditions (Fig. 9a). Spatially, a noticeable trend of increasing AOD from the northwest to the southeast is observed. This aligns with the transition from mountainous and forested terrain in the northwest to urban and agricultural areas in the southeast, where there are more industrial activities than in the northwest, known for its high density of intellectual workforce (e.g., universities and high-tech sector, the so-called China's Silicon Valley). The central core urban region experiences heavy haze pollution with much higher AOD levels (often >2), primarily due to the substantial release of pollutants from human activities. The spatial pattern of our retrieval closely resembles the general spatial pattern of the MAIAC AOD data. However, compared to MAIAC AOD products with a coarse resolution (~1 km), which contains only a few pixels within the city, Landsat AOD retrieval offers a more effective capture of pollution variations in urban areas by providing a much larger number of valid pixels due to its very higher resolution (~30 m). Significant discrepancies are observed at image-splicing points, indicated by red arrows, with an overestimated AOD value at the Beijing site (1.82 according to MAIAC compared to our 1.57 against the ground measurement of 1.61). Similarly, there is good agreement between our Landsat and MODIS MAIAC AOD retrievals during a heavy smog pollution event in urban and surrounding areas in Southeast Asia, specifically Chiang Mai, Thailand.

Our model demonstrates good performance in capturing natural high-pollution events, like regions in the US that experience frequent wildfires during the warm seasons. Two major forest wildfire events are seen in a single Landsat image in the western US, showing the exceptionally high AOD values within the core smoke region of the wildfires, as well as the surrounding areas affected by the transmission of smoke particles (Fig. 9c). By contrast, MAIAC AOD retrievals over the core pyrotechnic area are missing because these black pixels are identified as clouds. Another example is the Sahara Desert, located in northern Africa, which is comprised of rocky deserts and sand dunes. It has low vegetation cover and limited human activities, making it prone to dust storms in spring. Our model captures a large dust track with high AOD concentrations running from the southwest to the northeast in the image, with the dust distribution closely aligning with the true color image, particularly noticeable in the tail end of the dust track in the north (Fig. 9d). Although showing a similar spatial pattern, MAIAC tends to overlook the high AODs in the core dust source area in the southeast and underestimates the AOD in areas affected by thin dust (red arrows). Note that the spatial distribution differences also arise from variations in the transit time of the two satellites (often exceeding half an hour). Such spatial disparities tend to be more pronounced for pollutants with shorter life cycles, such as those emitted by fires and dust, compared to those with longer life cycles, like haze and smog. Nevertheless, Landsat AOD retrieval can be sensitive to changes in land surface reflectance and surface textures due to very high spatial resolution. While these impacts are present, they are relatively minor and unavoidable.

3.3.3. Comparison with other AI models, physical algorithms, and studies

Finally, we compare the performance of our model with currently popular AI models by conducting the same trial-and-error process to determine optimal parameters for each model, and evaluating them with the same inputs through spatiotemporally independent validation, i.e., training these models on data from 2015 to 2020 and validating them on data from the remaining years (Table 3). All widely used tree-based ML models perform well in retrieving global AOD levels, showing good correlations with surface observations ($R = 0.73–0.84$), average MAEs and RMSEs generally below 0.08 and 0.14, respectively, and a relatively high proportion of retrievals meeting the EE (> 64 %) and GCOS (> 33 %) criteria. Moreover, boosting-based models (i.e., XGBoost, CatBoost, and LightDBM) outperform bagging-based ensemble-learning methods (Extra Trees and Random Forest) in aerosol retrievals due to their continuous optimization functions, which correct residuals more effectively. However, DL, with its enhanced data-mining capabilities and improved ability to tackle nonlinear problems, exhibits improved accuracy, especially the latest models like MLP and ResNet (e.g., $R > 0.84$, $f_{EE} > 80$ %). The Transformer model, a recent, powerful, state-of-the-art DL approach, surpasses all other AI models across all evaluation metrics, attributed to its superior data-mining and processing capabilities. Specifically, R improved by 2 % to 17 %, RMSE decreased by 4 % to 28 %, and especially the median bias reduced by 57 % to 89 %. Similar enhancements are observed in the increased portions of retrievals that fall within the EE (by 3 %–21 %) and GCOS (by 6 %–62 %) error margins. The 10-CV results performed at sample, spatial, and temporal scales yield similar conclusions, further substantiating the superiority of the Transformer model (Table S7). Efficiency tests are also conducted among various AI models. Tree-based ML models are known for their fast training speeds and lower memory consumption. However, DL models, while less efficient, typically require several minutes for training and have memory usage below 2 GB. Transformer, due to its more complex structures, requires longer training times, but the process remains relatively brief, taking approximately 244 s (about 4 min). Notably, the model needs to be trained only once for any application, which is acceptable on a global scale.

Also conducted are comparisons with outputs or operational products derived from conventional algorithms and other studies utilizing AI models to retrieve AOD from Landsat imagery at a global scale (Table 4). Our model is slightly more accurate (e.g., $R = 0.905$, $f_{EE} = 85.96$ %) and ~ 33 times higher in spatial resolution than the widely used MODIS MAIAC algorithm (e.g., $R = 0.878$, $f_{EE} = 83.62$ %), which provides a 1-km AOD product covering the land (Lyapustin et al., 2018). However, there are no Landsat MAIAC AOD products available, and in principle, the MAIAC algorithm cannot be applied to Landsat imagery since it requires a high-frequency (e.g., daily) time series of images to determine surface reflectance for short-wavelength channels. Additionally, our model surpasses the performance of two highly regarded Landsat ACIX-II Land algorithms (Doxani et al., 2023), including the Image correction for atmospheric effects (iCOR) (De Keukelaere et al., 2018) and Land Surface Reflectance Code (LaSRC) (Vermote et al., 2016, 2018). Note that while these algorithms are utilized for generating Landsat surface

Table 3
Comparison of performances of various machine- and deep-learning models for retrieving AOD from Landsat imagery.

Category	Model	R	Median Bias	MAE	RMSE	= EE (%)	= GCOS (%)	Training Speed (s)	Training memory (MB)
Tree-based Machine Learning	Extra Trees	0.739	0.027	0.074	0.131	68.51	31.72	0.33	13.38
	Random Forest	0.779	0.019	0.065	0.118	74.46	39.97	1.20	26.88
	XGBoost	0.832	0.008	0.058	0.103	79.15	47.45	2.17	15.23
	CatBoost	0.836	0.007	0.058	0.102	78.81	47.13	1.93	10.97
	LightGBM	0.838	0.008	0.058	0.101	79.35	46.66	6.83	35.75
Deep Learning	DBN	0.833	0.008	0.062	0.104	76.44	43.14	213.81	1926.12
	LSTM	0.838	0.009	0.059	0.101	78.42	43.83	823.25	1116.49
	MLP	0.848	0.010	0.056	0.098	80.31	46.33	71.38	1921.89
	ResNet	0.849	0.012	0.057	0.099	80.61	48.36	75.48	1921.97
	Transformer	**0.866**	**0.003**	**0.054**	**0.094**	**82.65**	**51.49**	**244.31**	**1922.24**

Table 4

Comparison of overall accuracies between conventional algorithms and AI models for retrieving global AOD from previous studies.

Model	R	RMSE	MAE	= EE (%)	= GCOS (%)	Sensor	Reference
MAIAC	0.878	0.080	0.048	83.62	51.26	MODIS	Lyapustin et al. (2018)
iCOR	0.826	0.139	–	–	–	Landsat	Doxani et al. (2023)
LaSRC	0.832	0.141	–	–	–	Landsat	Doxani et al. (2023)
ERF	0.883	0.090	0.047	85.23	–	Landsat	Liang et al. (2022)
DNN	0.900	0.120	0.080	71.91	–	Landsat	She et al. (2022)
AeroTrans	0.905	0.083	0.048	85.96	54.55	Landsat	This study

DNN: Deep neural network; ERF: Extremely randomized trees; iCOR: Image correction for atmospheric effects; LaSRC: Land Surface Reflectance Code; MAIAC: Multi-Angle Implementation of Atmospheric Correction.

reflectance products, their AOD outputs are not publicly accessible, restricting access to experts who can effectively utilize these intricate codes and software for AOD retrievals. As a result, many researchers have developed their own AOD retrieval algorithms for Landsat imagery, but most are confined to local (urban) regions (Kumar and Mehta, 2023; Lin et al., 2021a; Tian et al., 2018). Currently, there are very few global Landsat aerosol retrieval studies due to the massive amount of data involved. In comparison to the two available global aerosol retrieval studies using extremely randomized trees (ERF; Liang et al., 2022) and the deep neural network (DNN; She et al., 2022) models (note that the accuracy may vary slightly from different sites and time periods), our model has a higher overall accuracy, marked by increased agreements and reduced uncertainties.

4. Summary and conclusions

The Landsat series of satellites provide Earth observations dating back to the 1970s, with a high spatial resolution of 30 m every 16 days, making them highly valuable for a variety of applications, such as land use/cover classification and change detection, resource assessment, and environmental monitoring. In this study, we introduce the Transformer deep-learning model to address numerous intractable nonlinear problems inherent in the complex processes of decoupling the Earth-atmosphere system and retrieving AOD over land from Landsat imagery, called the AeroTrans-Landsat model. All Landsat data preprocessing, spatiotemporal matching, and aerosol retrieval tasks are efficiently executed by integrating the Google Earth Engine (GEE) and Colaboratory (Colab) cloud platforms. In this effort, the study gathers all available images (~22,280 cloud-screened scenes) from Landsat 8 and 9, spanning from their launch to 2022, matching approximately 560 ground monitoring stations. They are then used to develop a robust model capable of conducting global aerosol retrieval tasks for Landsat imagery in an automatic and operational manner.

We utilize the XAI (eXplainable Artificial Intelligence)-SHAP (SHapley Additive exPlanations) method to elucidate the internal mechanisms of our model, revealing the significance of multi-band spectral channels and observation geometry in aerosol retrieval, contributing 80 % and 11 %, respectively. Overall, our model shows good performance in retrieving AOD, as indicated by the average sample-based, spatial-based, and temporal-based cross-validation correlation coefficients (R) (root-mean-square error, RMSE) of 0.905 (0.083), 0.845 (0.104), and 0.876 (0.094), respectively. Moreover, independent spatiotemporal validations demonstrate the model's good ability to retrieve AOD levels for new dates and locations (e.g., $R =$ 0.866, RMSE = 0.094). Aerosol retrieval experiments conducted in typical clear and polluted regions worldwide illustrate the model's capacity to capture detailed variations in AOD across surfaces with varying reflectance properties, particularly in urban areas. Our study provides a new approach of obtaining high-resolution AOD retrieval using AI from Landsat imagery over land, offering valuable insights into environmental and air quality assessments. We acknowledge that traditional aerosol retrieval algorithms based on the radiative transfer model for Landsat 8 and other sensors like MODIS could be more independent because they do not rely on ground-based observations. However, these

methods have many assumptions, such as inaccuracies in aerosol-type assumptions (mostly fixed) and estimates of surface reflectance. In contrast, the AI-driven method provides alternative retrievals that complement the traditional methods in their strengths and weaknesses, aiming to maximize the use of available information by incorporating both space and ground-based observations to better constrain certain ill-posed retrievals, although this may come at the expense of sacrificing some degree of redeem.

Despite achieving acceptable performance, the uneven distribution of ground stations, especially in regions with few sites (like high-latitude areas, Central and East Asia, North Africa, and the Middle East), could impact the global adaptability of the AeroTrans-Landsat model. This global aerosol retrieval model can also be affected by a limited number of samples under high pollution conditions, potentially leading to increased uncertainties in scenarios with high AOD, such as haze, smog, dust, and forest fires. In our future work, we will explore the possibility of incorporating simulated samples or introducing additional observation networks to increase the number of global samples, especially under high-pollution conditions, with the aim of enhancing the model's global modeling capability.

CRediT authorship contribution statement

Jing Wei: Writing – review & editing, Writing – original draft, Methodology, Formal analysis, Data curation, Conceptualization. **Zhihui Wang:** Writing – original draft, Validation, Methodology, Formal analysis, Data curation. **Zhanqing Li:** Writing – review & editing, Supervision, Funding acquisition. **Zhengqiang Li:** Writing – review & editing, Data curation. **Shulin Pang:** Formal analysis, Data curation. **Xinyuan Xi:** Formal analysis, Data curation. **Maureen Cribb:** Writing – review & editing. **Lin Sun:** Writing – review & editing, Supervision, Funding acquisition.

Declaration of competing interest

The authors declare that they have no conflict of interest.

Data availability

The developed Transformer-informed global aerosol retrieval online framework for Landsat imagery (AeroTrans-Landsat) will be available upon request.

Acknowledgments

Appendix A. Supplementary data

Supplementary data to this article can be found online at https://doi.org/10.1016/j.rse.2024.114404.

References

Chen, Q., Miao, R., Geng, G., Shrivastava, M., Dao, X., Xu, B., Sun, J., Zhang, X., Liu, M., Tang, G., Tang, Q., Hu, H., Huang, R.-J., Wang, H., Zheng, Y., Qin, Y., Guo, S., Hu, M., Zhu, T., 2024. Widespread 2013–2020 decreases and reduction challenges of organic aerosol in China. Nat. Commun. 15, 4465.

Crawford, C.J., Roy, D.P., Arab, S., Barnes, C., Vermote, E., Hulley, G., Gerace, A., Choate, M., Engebretson, C., Micijevic, E., Schmidt, G., Anderson, C., Anderson, M., Bouchard, M., Cook, B., Dittmeier, R., Howard, D., Jenkerson, C., Kim, M., Kleyians, T., Maiersperger, T., Mueller, C., Neigh, C., Owen, L., Page, B., Pahlevan, N., Rengarajan, R., Roger, J.-C., Sayler, K., Scaramuzza, P., Skakun, S., Yan, L., Zhang, H.K., Zhu, Z., Zahn, S., 2023. The 50-year Landsat collection 2 archive. Sci. Remote Sens. 8, 100103.

De Keukelaere, L., Sterckx, S., Adriaensen, S., Knaeps, E., Reusen, I., Giardino, C., Bresciani, M., Hunter, P., Neil, C., Van der Zande, D., Vaiciute, D., 2018. Atmospheric correction of Landsat-8/OLI and Sentinel-2/MSI data using iCOR algorithm: validation for coastal and inland waters. Eur. J. Remote Sens. 51, 525–542.

Dong, X., Bao, J., Chen, D., Zhang, W., Yu, N., Yuan, L., Chen, D., Guo, B., 2022. Cswin transformer: A general vision transformer backbone with cross-shaped windows. In: Proceedings of the IEEE/CVF Conference on Computer Vision and Pattern Recognition, pp. 12124–12134.

Dosovitskiy, A., Beyer, L., Kolesnikov, A., Weissenborn, D., Zhai, X., Unterthiner, T., Dehghani, M., Minderer, M., Heigold, G., Gelly, S., Uszkoreit, J., Houlsby, N., 2021. An Image is Worth 16x16 Words: transformers for image recognition at scale. In: Proceedings of the 9th International Conference on Learning Representations. Vienna, Austria.

Doxani, G., Vermote, E., Roger, J.C., Gascon, F., Adriaensen, S., Frantz, D., Vanhellemont, Q., 2018. Atmospheric correction inter-comparison exercise. Remote Sens. 10 (2), 352.

Doxani, G., Vermote, E.F., Roger, J.-C., Skakun, S., Gascon, F., Collison, A., De Keukelaere, L., Desjardins, C., Frantz, D., Hagolle, O., Kim, M., Louis, J., Pacifici, F., Pflug, B., Poilvé, H., Ramon, D., Richter, R., Yin, F., 2023. Atmospheric Correction Inter-comparison eXercise, ACIX-II Land: an assessment of atmospheric correction processors for Landsat 8 and Sentinel-2 over land. Remote Sens. Environ. 285, 113412.

Estellés, V., Campanelli, M., Utrillas, M.P., Expósito, F., Martínez-Lozano, J.A., 2012. Comparison of AERONET and SKYRAD4.2 inversion products retrieved from a Cimel CE318 sunphotometer. Atmos. Meas. Tech. 5, 569–579.

Falah, S., Mhawish, A., Sorek-Hamer, M., Lyapustin, A.I., Kloog, I., Banerjee, T., Kizel, F., Broday, D.M., 2021. Impact of environmental attributes on the uncertainty in MAIAC/MODIS AOD retrievals: A comparative analysis. Atmos. Environ. 262, 118659.

Fuller, R., Landrigan, P.J., Balakrishnan, K., Bathan, G., Bose-O`Reilly, S., Brauer, M., Caravanos, J., Chiles, T., Cohen, A., Corra, L., Cropper, M., Ferraro, G., Hanna, J., Hanrahan, D., Hu, H., Hunter, D., Janata, G., Kupka, R., Lanphear, B., Lichtveld, M., Martin, K., Mustapha, A., Sanchez-Triana, E., Sandilya, K., Schaefli, L., Shaw, J., Seddon, J., Suk, W., Téllez-Rojo, M.M., Yan, C., 2022. Pollution and health: a progress update. Lancet Planet. Health 6, e535–e547.

Fuzzi, S., Baltensperger, U., Carslaw, K., Decesari, S., Denier van der Gon, H., Facchini, M.C., Fowler, D., Koren, I., Langford, B., Lohmann, U., Nemitz, E., Pandis, S., Riipinen, I., Rudich, Y., Schaap, M., Slowik, J.G., Spracklen, D.V., Vignati, E., Wild, M., Williams, M., Gilardoni, S., 2015. Particulate matter, air quality and climate: lessons learned and future needs. Atmos. Chem. Phys. 15, 8217–8299.

GCOS, 2010. Systematic Observation Requirements for Satellite-Based Products for Climate, 2011 Update, Supplemental Details to the Satellite-Based Component of the Implementation Plan for the Global Observing System for Climate in Support of the UNFCCC (2010 Update). Global Climate Observing System, World Meteorological Organization, Geneva.

Giles, D.M., Sinyuk, A., Sorokin, M.G., Schafer, J.S., Smirnov, A., Slutsker, I., Eck, T.F., Holben, B.N., Lewis, J.R., Campbell, J.R., Welton, E.J., Korkin, S.V., Lyapustin, A.I., 2019. Advancements in the Aerosol Robotic Network (AERONET) Version 3 database – automated near-real-time quality control algorithm with improved cloud screening for Sun photometer aerosol optical depth (AOD) measurements. Atmos. Meas. Tech. 12, 169–209.

Gorelick, N., Hancher, M., Dixon, M., Ilyushchenko, S., Thau, D., Moore, R., 2017. Google Earth Engine: planetary-scale geospatial analysis for everyone. Remote Sens. Environ. 202, 18–27.

Gunthe, S.S., Liu, P., Panda, U., Raj, S.S., Sharma, A., Darbyshire, E., Reyes-Villegas, E., Allan, J., Chen, Y., Wang, X., Song, S., Pöhlker, M.L., Shi, L., Wang, Y., Kommula, S. M., Liu, T., Ravikrishna, R., McFiggans, G., Mickley, L.J., Martin, S.T., Pöschl, U., Andreae, M.O., Coe, H., 2021. Enhanced aerosol particle growth sustained by high continental chlorine emission in India. Nat. Geosci. 14, 77–84.

He, L., Wang, L., Li, Z., Jiang, D., Sun, L., Liu, D., Liu, L., Yao, H., Zhou, Z., Wei, J., 2021. VIIRS Environmental Data Record and Deep Blue aerosol products: validation, comparison, and spatiotemporal variations from 2013 to 2018 in China. Atmos. Environ. 250, 118265.

Holben, B.N., Eck, T.F., Slutsker, I., Tanré, D., Buis, J.P., Setzer, A., Vermote, E., Reagan, J.A., Kaufman, Y.J., Nakajima, T., Lavenu, F., Jankowiak, I., Smirnov, A., 1998. AERONET—A federated instrument network and data archive for aerosol characterization. Remote Sens. Environ. 66, 1–16.

Hsu, N.C., Jeong, M.-J., Bettenhausen, C., Sayer, A.M., Hansell, R., Seftor, C.S., Huang, J., Tsay, S.-C., 2013. Enhanced Deep Blue aerosol retrieval algorithm: the second generation. J. Geophys. Res. Atmos. 118, 9296–9315.

Jia, C., Sun, L., Chen, Y., Liu, Q., Yu, H., Zhang, W., 2022. Satellite aerosol retrieval using scene simulation and deep belief network. IEEE Trans. Geosci. Remote Sens. 60, 1–16.

Kaufman, Y.J., Tanré, D., Gordon, H.R., Nakajima, T., Lenoble, J., Frouin, R., Grassl, H., Herman, B.M., King, M.D., Teillet, P.M., 1997. Passive remote sensing of tropospheric aerosol and atmospheric correction for the aerosol effect. J. Geophys. Res. Atmos. 102, 16,815–16,830.

Kaufman, Y.J., Tanré, D., Boucher, O., 2002. A satellite view of aerosols in the climate system. Nature 419, 215–223.

Kim, K.-H., Kabir, E., Kabir, S., 2015. A review on the human health impact of airborne particulate matter. Environ. Int. 74, 136–143.

Kumar, A., Mehta, M., 2023. Investigating the applicability of a simple iterative approach for aerosol optical depth (AOD) retrieval over diverse land surface types from Landsat 8 and Sentinel 2 using visible and near-infrared (VNIR) spectral bands. Atmos. Environ. 314, 120082.

Levy, R.C., Mattoo, S., Munchak, L.A., Remer, L.A., Sayer, A.M., Patadia, F., Hsu, N.C., 2013. The Collection 6 MODIS aerosol products over land and ocean. Atmos. Meas. Tech. 6, 2989–3034.

Li, Z., Zhao, X., Kahn, R., Mishchenko, M., Remer, L., Lee, K.H., Wang, M., Laszlo, I., Nakajima, T., Maring, H., 2009. Uncertainties in satellite remote sensing of aerosols and impact on monitoring its long-term trend: a review and perspective. Ann. Geophys. 27, 2755–2770.

Li, Z., Niu, F., Fan, J., Liu, Y., Rosenfeld, D., Ding, Y., 2011. Long-term impacts of aerosols on the vertical development of clouds and precipitation. Nat. Geosci. 4, 888–894.

Li, Z., Guo, J., Ding, A., Liao, H., Liu, J., Sun, Y., Wang, T., Xue, H., Zhang, H., Zhu, B., 2017. Aerosol and boundary-layer interactions and impact on air quality. Natl. Sci. Rev. 4, 810–833.

Li, Z.Q., Xu, H., Li, K.T., Li, D.H., Xie, Y.S., Li, L., Zhang, Y., Gu, X.F., Zhao, W., Tian, Q.J., Deng, R.R., Su, X.L., Huang, B., Qiao, Y.L., Cui, W.Y., Hu, Y., Gong, C.L., Wang, Y.Q., Wang, X.F., Wang, J.P., Du, W.B., Pan, Z.Q., Li, Z.Z., Bu, D., 2018. Comprehensive study of optical, physical, chemical, and radiative properties of total columnar atmospheric aerosols over China: an overview of Sun–Sky Radiometer Observation Network (SONET) measurements. Bull. Am. Meteor. Soc. 99, 739–755.

Li, S., Wang, W., Hashimoto, H., Xiong, J., Vandal, T., Yao, J., Qian, L., Ichii, K., Lyapustin, A., Wang, Y., Nemani, R., 2019a. First provisional land surface reflectance product from geostationary satellite Himawari-8 AHI. Remote Sens. 11, 2990.

Li, Z., Roy, D.P., Zhang, H.K., Vermote, E.F., Huang, H., 2019b. Evaluation of Landsat-8 and Sentinel-2A aerosol optical depth retrievals across Chinese cities and implications for medium spatial resolution urban aerosol monitoring. Remote Sens. 11, 122.

Li, J., Wong, M.S., Lee, K.H., Nichol, J.E., Abbas, S., Li, H., Wang, J., 2022. A physical knowledge-based machine learning method for near-real-time dust aerosol properties retrieval from the Himawari-8 satellite data. Atmos. Environ. 280, 119098.

Liang, T., Liang, S., Zou, L., Sun, L., Li, B., Lin, H., He, T., Tian, F., 2022. Estimation of aerosol optical depth at 30 m resolution using Landsat imagery and machine learning. Remote Sens. 14, 1053.

Lin, H., Li, S., Xing, J., He, T., Yang, J., Wang, Q., 2021a. High resolution aerosol optical depth retrieval over urban areas from Landsat-8 OLI images. Atmos. Environ. 261, 118591.

Lin, H., Li, S., Xing, J., Yang, J., Wang, Q., Dong, L., Zeng, X., 2021b. Fusing retrievals of high resolution aerosol optical depth from Landsat-8 and Sentinel-2 observations over urban areas. Remote Sens. 13, 4140.

Liu, Y., Lapata, M., 2019. Text summarization with pretrained encoders. In: Proceedings of the 2019 Conference on Empirical Methods in Natural Language Processing and the 9th International Joint Conference on Natural Language Processing, pp. 3730–3740. Hong Kong, China.

Lundberg, S.M., Lee, S.-I., 2017. A unified approach to interpreting model predictions. In: Proceedings of the 31st International Conference on Neural Information Processing Systems. Curran Associates Inc., Long Beach, California, USA, pp. 4768–4777.

Luo, N., Wong, M.S., Zhao, W., Yan, X., Xiao, F., 2015. Improved aerosol retrieval algorithm using Landsat images and its application for PM$_{10}$ monitoring over urban areas. Atmos. Res. 153, 264–275.

Lyapustin, A., Wang, Y., Korkin, S., Huang, D., 2018. MODIS Collection 6 MAIAC algorithm. Atmos. Meas. Tech. 11, 5741–5765.

Ma, Z., Dey, S., Christopher, S., Liu, R., Bi, J., Balyan, P., Liu, Y., 2022. A review of statistical methods used for developing large-scale and long-term PM$_{2.5}$ models from satellite data. Remote Sens. Environ. 269, 112827.

Masek, J.G., Wulder, M.A., Markham, B., McCorkel, J., Crawford, C.J., Storey, J., Jenstrom, D.T., 2020. Landsat 9: empowering open science and applications through continuity. Remote Sens. Environ. 248, 111968.

Nakajima, T., Campanelli, M., Che, H., Estellés, V., Irie, H., Kim, S.W., Kim, J., Liu, D., Nishizawa, T., Pandithurai, G., Soni, V.K., Thana, B., Tugjsurn, N.U., Aoki, K., Go, S., Hashimoto, M., Higurashi, A., Kazadzis, S., Khatri, P., Kouremeti, N., Kudo, R., Marenco, F., Momoi, M., Ningombam, S.S., Ryder, C.L., Uchiyama, A., Yamazaki, A., 2020. An overview of and issues with sky radiometer technology and SKYNET. Atmos. Meas. Tech. 13, 4195–4218.

Paszke, A., Gross, S., Massa, F., Lerer, A., Bradbury, J., Chanan, G., Killeen, T., Lin, Z., Gimelshein, N., Antiga, L., Desmaison, A., Köpf, A., Yang, E., DeVito, Z., Raison, M., Tejani, A., Chilamkurthy, S., Steiner, B., Fang, L., Bai, J., Chintala, S., 2019. PyTorch: an imperative style, high-performance deep learning library. In: Proceedings of the 33rd Conference on Neural Information Processing Systems. Curran Associates Inc., Vancouver, Canada, pp. 8024–8035.

Ramanathan, V., Crutzen, P.J., Kiehl, J.T., Rosenfeld, D., 2001. Aerosols, climate, and the hydrological cycle. Science 294, 2119–2124.

Rodriguez, J.D., Perez, A., Lozano, J.A., 2010. Sensitivity analysis of k-fold cross validation in prediction error estimation. IEEE Trans. Pattern Anal. 32, 569–575.

Rosenfeld, D., Sherwood, S., Wood, R., Donner, L., 2014. Climate effects of aerosol-cloud interactions. Science 343, 379–380.

Roy, D.P., Wulder, M.A., Loveland, T.R., CE, W., Allen, R.G., Anderson, M.C., Helder, D., Irons, J.R., Johnson, D.M., Kennedy, R., Scambos, T.A., Schaaf, C.B., Schott, J.R., Sheng, Y., Vermote, E.F., Belward, A.S., Bindschadler, R., Cohen, W.B., Gao, F., Hipple, J.D., Hostert, P., Huntington, J., Justice, C.O., Kilic, A., Kovalskyy, V., Lee, Z. P., Lymburner, L., Masek, J.G., McCorkel, J., Shuai, Y., Trezza, R., Vogelmann, J., Wynne, R.H., Zhu, Z., 2014. Landsat-8: science and product vision for terrestrial global change research. Remote Sens. Environ. 145, 154–172.

She, L., Zhang, H., Wang, W., Wang, Y., Shi, Y., 2019. Evaluation of the Multi-Angle Implementation of Atmospheric Correction (MAIAC) aerosol algorithm for Himawari-8 data. Remote Sens. 11, 2771.

She, L., Zhang, H.K., Bu, Z., Shi, Y., Yang, L., Zhao, J., 2022. A deep-neural-network-based aerosol optical depth (AOD) retrieval from Landsat-8 top of atmosphere data. Remote Sens. 14, 1411.

She, L., Li, Z., de Leeuw, G., Wang, W., Wang, Y., Yang, L., Shi, Y., 2024. Time series retrieval of Multi-wavelength Aerosol optical depth by adapting Transformer (TMAT) using Himawari-8 AHI data. Remote Sens. Environ. 305, 114115.

Sogacheva, L., Popp, T., Sayer, A.M., Dubovik, O., Garay, M.J., Heckel, A., Hsu, N.C., Jethva, H., Kahn, R.A., Kolmonen, P., Kosmale, M., de Leeuw, G., Levy, R.C., Litvinov, P., Lyapustin, A., North, P., Torres, O., Arola, A., 2020. Merging regional and global aerosol optical depth records from major available satellite products. Atmos. Chem. Phys. 20, 2031–2056.

Su, T., Laszlo, I., Li, Z., Wei, J., Kalluri, S., 2020. Refining aerosol optical depth retrievals over land by constructing the relationship of spectral surface reflectances through deep learning: application to Himawari-8. Remote Sens. Environ. 251, 112093.

Sun, L., Wei, J., Bilal, M., Tian, X., Jia, C., Guo, Y., Mi, X., 2016. Aerosol optical depth retrieval over bright areas using Landsat 8 OLI images. Remote Sens. 8, 23.

Sun, H., Shin, Y., Xia, M., Ke, S., Wan, M., Yuan, L., Guo, Y., Archibald, A., 2022. Spatial resolved surface ozone with urban and rural differentiation during 1990–2019: A space-time Bayesian Neural Network downscaler. Environ. Sci. Technol. 56 (11), 7337–7349.

Tamiminia, H., Salehi, B., Mahdianpari, M., Quackenbush, L., Adeli, S., Brisco, B., 2020. Google Earth Engine for geo-big data applications: a meta-analysis and systematic review. ISPRS J. Photogramm. Remote Sens. 164, 152–170.

Tao, M., Chen, J., Xu, X., Man, W., Xu, L., Wang, L., Wang, Y., Wang, J., Fan, M., Shahzad, M.I., Chen, L., 2023. A robust and flexible satellite aerosol retrieval algorithm for multi-angle polarimetric measurements with physics-informed deep learning method. Remote Sens. Environ. 297, 113763.

Tian, X., Liu, Q., Song, Z., Dou, B., Li, X., 2018. Aerosol optical depth retrieval from Landsat 8 OLI images over urban areas supported by MODIS BRDF/Albedo data. IEEE Geosci. Remote Sens. Lett. 15, 976–980.

Vaswani, A., Shazeer, N., Parmar, N., Uszkoreit, J., Jones, L., Gomez, A.N., Kaiser, Ł., Polosukhin, I., 2017. Attention is all you need. In: Proceedings of the 31st International Conference on Neural Information Processing Systems. Curran Associates Inc., Long Beach, California, USA, pp. 6000–6010.

Vermote, E., Justice, C., Claverie, M., Franch, B., 2016. Preliminary analysis of the performance of the Landsat 8/OLI land surface reflectance product. Remote Sens. Environ. 185, 46–56.

Vermote, E., Roger, J.C., Franch, B., Skakun, S., 2018. LaSRC (Land Surface Reflectance Code): overview, application and validation using MODIS, VIIRS, LANDSAT and Sentinel 2 data's. In: IGARSS 2018–2018 IEEE International Geoscience and Remote Sensing Symposium, pp. 8173–8176.

Wang, Y., Yuan, Q., Li, T., Shen, H., Zheng, L., Zhang, L., 2019. Evaluation and comparison of MODIS Collection 6.1 aerosol optical depth against AERONET over regions in China with multifarious underlying surfaces. Atmos. Environ. 200, 280–301.

Wang, W., Wang, Y., Lyapustin, A., Hashimoto, H., Park, T., Michaelis, A., Nemani, R., 2022. A novel atmospheric correction algorithm to exploit the diurnal variability in hypertemporal geostationary observations. Remote Sens. 14, 964.

Wei, J., Huang, B., Sun, L., Zhang, Z., Wang, L., Bilal, M., 2017. A simple and universal aerosol retrieval algorithm for Landsat series Images over complex surfaces. J. Geophys. Res. Atmos. 122, 13,338–13,355.

Wei, J., Sun, L., Peng, Y., Wang, L., Zhang, Z., Bilal, M., Ma, Y., 2018. An improved high-spatial-resolution aerosol retrieval algorithm for MODIS images over land. J. Geophys. Res. Atmos. 123, 12,291–12,307.

Wei, J., Li, Z., Peng, Y., Sun, L., 2019a. MODIS Collection 6.1 aerosol optical depth products over land and ocean: validation and comparison. Atmos. Environ. 201, 428–440.

Wei, J., Li, Z., Sun, L., Peng, Y., Zhang, Z., Li, Z., Su, T., Feng, L., Cai, Z., Wu, H., 2019b. Evaluation and uncertainty estimate of next-generation geostationary meteorological Himawari-8/AHI aerosol products. Sci. Total Environ. 692, 879–891.

Wei, J., Li, Z., Sun, L., Peng, Y., Liu, L., He, L., Qin, W., Cribb, M., 2020a. MODIS Collection 6.1 3-km resolution aerosol optical depth product: global evaluation and uncertainty analysis. Atmos. Environ. 240, 117768.

Wei, X., Chang, N.-B., Bai, K., Gao, W., 2020b. Satellite remote sensing of aerosol optical depth: advances, challenges, and perspectives. Crit. Rev. Environ. Sci. Technol. 50, 1640–1725.

Wei, J., Li, Z., Lyapustin, A., Sun, L., Peng, Y., Xue, W., Su, T., Cribb, M., 2021. Reconstructing 1-km-resolution high-quality PM$_{2.5}$ data records from 2000 to 2018 in China: spatiotemporal variations and policy implications. Remote Sens. Environ. 252, 112136.

Wei, J., Li, Z., Lyapustin, A., Wang, J., Dubovik, O., Schwartz, J., Sun, L., Li, C., Liu, S., Zhu, T., 2023. First close insight into global daily gapless 1 km PM$_{2.5}$ pollution, variability, and health impact. Nat. Commun. 14, 8349.

Wulder, M.A., Loveland, T.R., Roy, D.P., Crawford, C.J., Masek, J.G., Woodcock, C.E., Allen, R.G., Anderson, M.C., Belward, A.S., Cohen, W.B., Dwyer, J., Erb, A., Gao, F., Griffiths, P., Helder, D., Hermosilla, T., Hipple, J.D., Hostert, P., Hughes, M.J., Huntington, J., Johnson, D.M., Kennedy, R., Kilic, A., Li, Z., Lymburner, L., McCorkel, J., Pahlevan, N., Scambos, T.A., Schaaf, C., Schott, J.R., Sheng, Y., Storey, J., Vermote, E., Vogelmann, J., White, J.C., Wynne, R.H., Zhu, Z., 2019. Current status of Landsat program, science, and applications. Remote Sens. Environ. 225, 127–147.

Wulder, M.A., Roy, D.P., Radeloff, V.C., Loveland, T.R., Anderson, M.C., Johnson, D.M., Healey, S., Zhu, Z., Scambos, T.A., Pahlevan, N., Hansen, M., Gorelick, N., Crawford, C.J., Masek, J.G., Hermosilla, T., White, J.C., Belward, A.S., Schaaf, C., Woodcock, C.E., Huntington, J.L., Lymburner, L., Hostert, P., Gao, F., Lyapustin, A., Pekel, J.-F., Strobl, P., Cook, B.D., 2022. Fifty years of Landsat science and impacts. Remote Sens. Environ. 280, 113195.

Yang, Y., Yang, K., Chen, Y., 2022. Aerosol retrieval algorithm for Sentinel-2 images over complex urban areas. IEEE Trans. Geosci. Remote Sens. 60, 1–9.

Yeom, J.M., Jeong, S., Ha, J.S., Lee, K.H., Lee, C.S., Park, S., 2022. Estimation of the hourly aerosol optical depth from GOCI geostationary satellite data: deep neural network, machine learning, and physical models. IEEE Trans. Geosci. Remote Sens. 60, 1–12.

Zhang, Y., Li, Z., Bai, K., Wei, Y., Xie, Y., Zhang, Y., Ou, Y., Cohen, J., Zhang, Y., Peng, Z., Zhang, X., Chen, C., Hong, J., Xu, H., Guang, J., Lv, Y., Li, K., Li, D., 2021. Satellite remote sensing of atmospheric particulate matter mass concentration: advances, challenges, and perspectives. Fundam. Res. 1, 240–258.